Supporting Information

A 2D flexible cobalt-MOF: reversible solid-state structural transformation, two-step and gate-opening adsorption behaviours, and selective adsorption of C_2H_2 over CO_2 and CH_4

Shan-Shan Wang, Yu-Jie Liang, Wei Guo, Yue Yin, Xiao-Yu Li, Quan-Qing Xu, Ai-Xin Zhu* and Bo Huang*

Faculty of Chemistry and Chemical Engineering, Yunnan Normal University, Kunming 650500, China.
E-mail: zaxchem@126.com (A.-X. Zhu) and huangbo15@foxmail.com (B. Huang).

Table of Contents

1. Materials and synthesis

All chemicals and solvents were obtained from commercial sources and used without further purification.

Synthesis of $[Co_3(ndc)_3(bimb)]\cdot 3DMF\cdot 2.5H_2O$ (Co-MOF-α).

A mixture of $Co(NO_3)_2\cdot 6H_2O$ (29 mg, 0.1 mmol), H_2ndc (22 mg, 0.1 mmol), bimb (16 mg, 0.05 mmol), DMF (4 mL) and HCl (0.04 mL, 1 mol/L) were placed in a 10 mL vial container and heated at 120 °C for 24 h, then cooled to room temperature at a rate of 5 °C/h. The blue-purple block crystals were collected by filtration, washed with DMF and dried under ambient condition. About 12.8 mg product was obtained (58.2 % yield based on H_2ndc). IR (cm^{-1}, KBr): 3427(w), 1668(s), 1609(s), 1582(s), 1497(m), 1402(s), 1358(w), 1198(w), 1092(m), 924(w), 789(s), 657(m), 482(m).

Synthesis of $[Co_3(ndc)_3(bimb)]$ (Co-MOF-β)

The single crystals and polycrystalline **Co-MOF-β** were obtained by heating of as-synthesized **Co-MOF-α** at 150 °C under vacuum for 12 h. IR (cm^{-1}, KBr): 3440(m), 1607(m), 1573(m), 1496(m), 1402(s), 1357(s), 1197(w), 1110(w), 1089(w), 923(m), 789(m), 655(w), 481(w).

2. Single-crystal X-ray diffraction measurement

Diffraction intensity of the **Co-MOF-α** was collected at room temperature on a Rigaku R-AXIS SPIDER diffractometer with graphite-monochromated Mo-Kα (λ = 0.71073 Å), and absorption correction was applied by using multi-scan program ABSCOR.[1] The crystal of **Co-MOF-α** is prone to lose the solvents to become opaque in air, so the crystal of Co-MOF-alpha was sealed immediately by AB glues. **Co-MOF-β** was performed on a D8 Venture diffractometer with graphite-monochromated Cu-Kα (λ = 1.54178 Å) radiation, and absorption correction was applied by using multi-scan program SADABS.[2] Both structures were first indexed in an C-centered monoclinic cell ($C2/c$ symmetry, For **Co-MOF-α**, a = 30.261(6) Å, b = 23.525(5) Å, c = 23.078(5) Å, β = 120.87(3)°; For **Co-MOF-α**, a = 27.7309(14) Å, b = 24.2649(11) Å, c = 22.3119(18) Å, β = 127.776(3)°). The structures was solved with direct methods and refined with a full-matrix least-squares technique with the SHELXTL program package[3] in this C-centered lattice. Anisotropic

thermal parameters were applied to all non-hydrogen atoms. Platon tests suggest that their space groups *C*2/*c* have alternate setting for standard *I*2/*a*, so their structures were finally described in the standard space group *I*2/*a*, after transformation of data into the I-centered lattice with a = 23.078(5) Å, b = 23.525(5) Å, c =27.050(12) Å, β = 106.21(3)° for **Co-MOF-α**, and a = 22.3119(18) Å, b = 24.2649(11) Å, c = 22.5563(15) Å, β = 103.654(6)° for **Co-MOF-β**. In **Co-MOF-α**, one of naphthalene moiety from ndc^{2-} ligands in the asymmetric unit is two-fold disorder, and all the disordered atoms in **Co-MOF-α** were refined in SHELX by using PART commands with free variables. Other commands SADI, DFIX, SIMU and FLAT were used to restrain the geometry of disorder ndc^{2-} moiety. The large volume fractions of disordered cations or solvents in the lattice pores could not be modelled in terms of atomic sites and were treated using the SQUEEZE routine in the PLATON software package.[4] The void volume (excluding guest molecules) in the crystal cell was calculated using the program PLATON.[4] The crystals of **Co-MOF-β** were obtained by heating the samples of **Co-MOF-α** at 150 degree, so the single-crystal quality of **Co-MOF-β** become quite poor because of phase transition after the removal of guests. The crystals of **Co- MOF-β** diffracted very weakly even if the diffraction data of **Co-MOF-β** was collected by using Cu-Kα radiation instead of Mo-Kα radiation with long exposure time (80 s) to obtain stronger diffraction data. However, no significant diffraction was observed above high two-theta degrees. Thus, some Alter A and B issues such as high R1, wR2 values, poor data / parameter ratio, very low resolution and completeness in the checkcif report occurred after the final refinement. Although some parameters after the final refinement are even beyond the ideal range, they do not affect the identification of the overall structure. In **Co-MOF-β**, one benzene moiety from bimb ligand in the asymmetric unit are two-fold disorder, and all the disordered atoms in **Co-MOF-β** were refined in SHELX using PART commands with free variables. Other commands SADI, DFIX, SIMU and FLAT were used to restrain the geometry of disorder moiety. CCDC 2202608-2202609 contain the supplementary crystallographic data for this paper. The plots of F_{obs} vs F_{cal}, I / $\sigma(I)$ vs resolution,

*R*merge vs resolution and ORTEP drawing for **Co-MOF-α** and **Co-MOF-β** are shown in Figure S1-S8. These data can be obtained free of charge from the Cambridge Crystallographic Data Centre via www.ccdc.cam.ac.uk/data_request/cif. Crystal data as well as details of data collection and refinement for **Co-MOF-α** and **Co-MOF-β** are summarized in Table S1 and the selected bond lengths and angles are listed in Table S2 and Table S3.

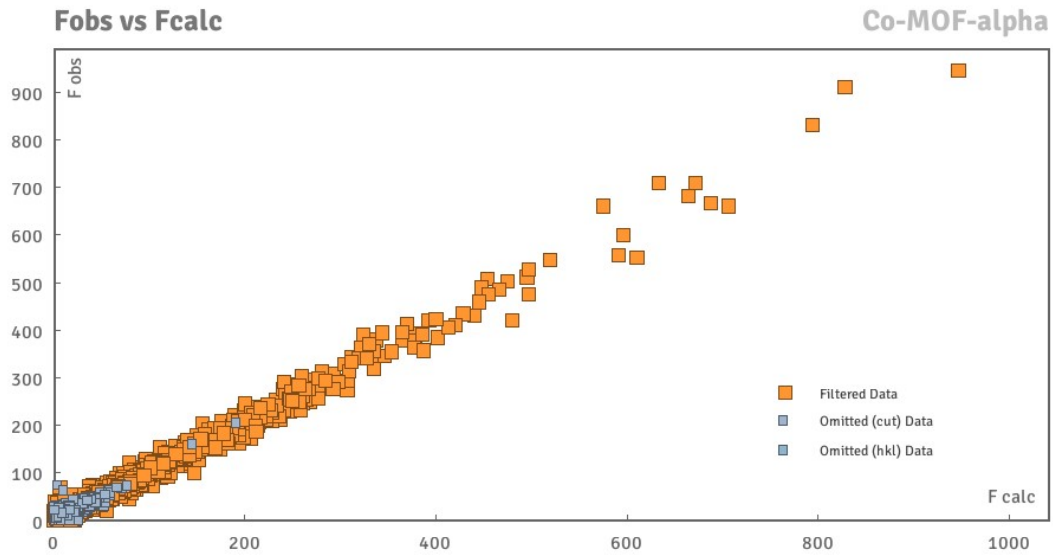

Figure S1. The plot of F_{obs} vs F_{cal} for **Co-MOF-α**.

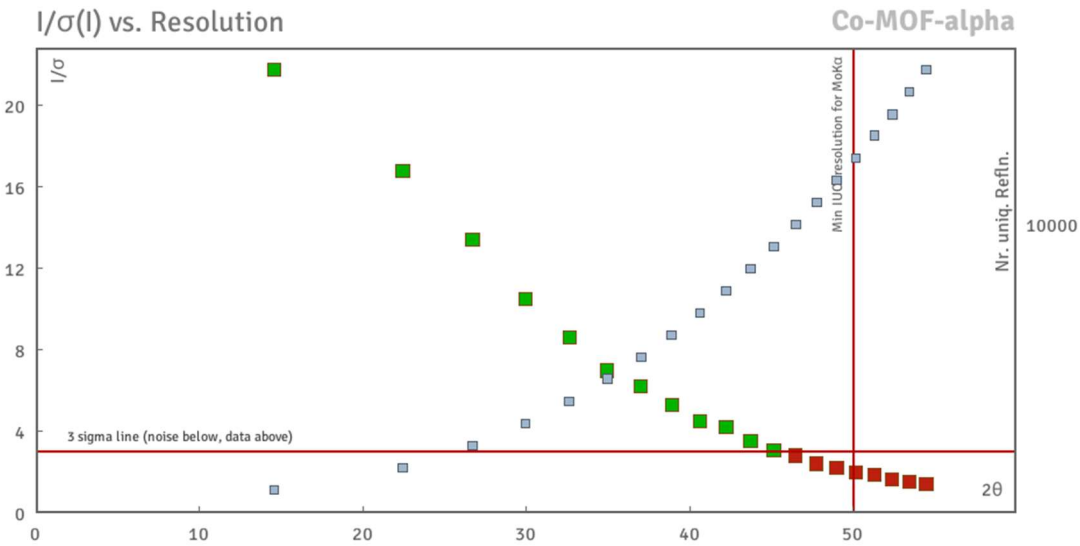

Figure S2. The plot of I / σ(I) vs resolution for **Co-MOF-α**.

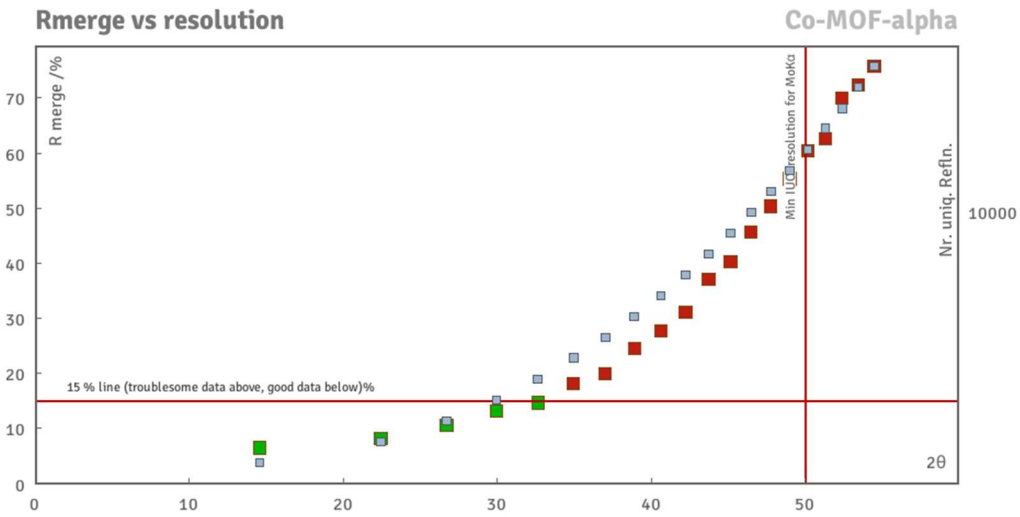

Figure S3. The plot of *R*merge vs resolution for **Co-MOF-*α***.

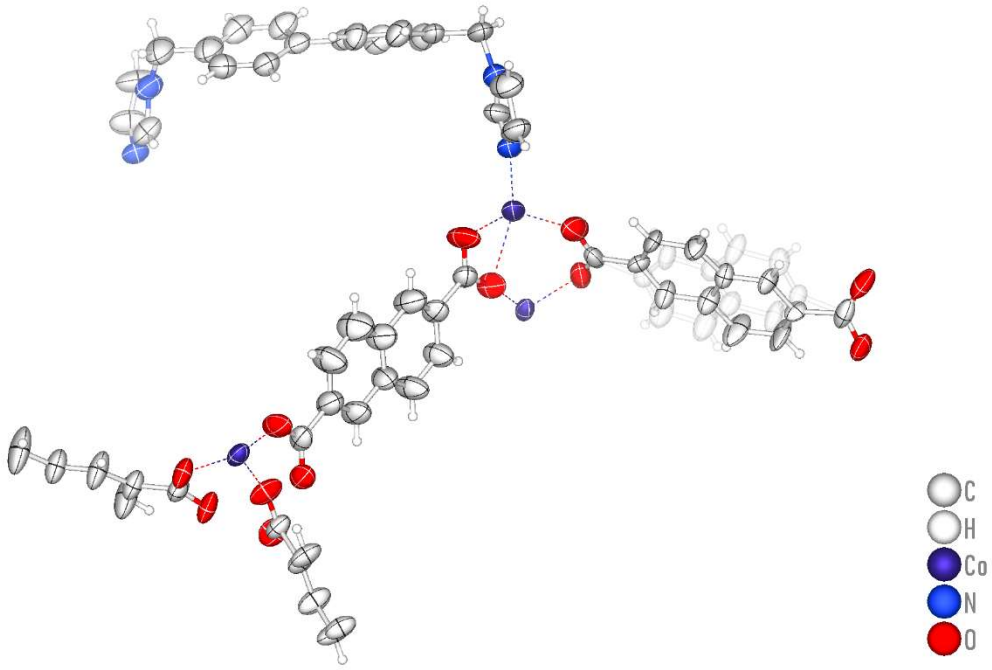

Figure S4. The ORTEP drawing showing thermal ellipsoids at 50% probability for **Co-MOF-*α***.

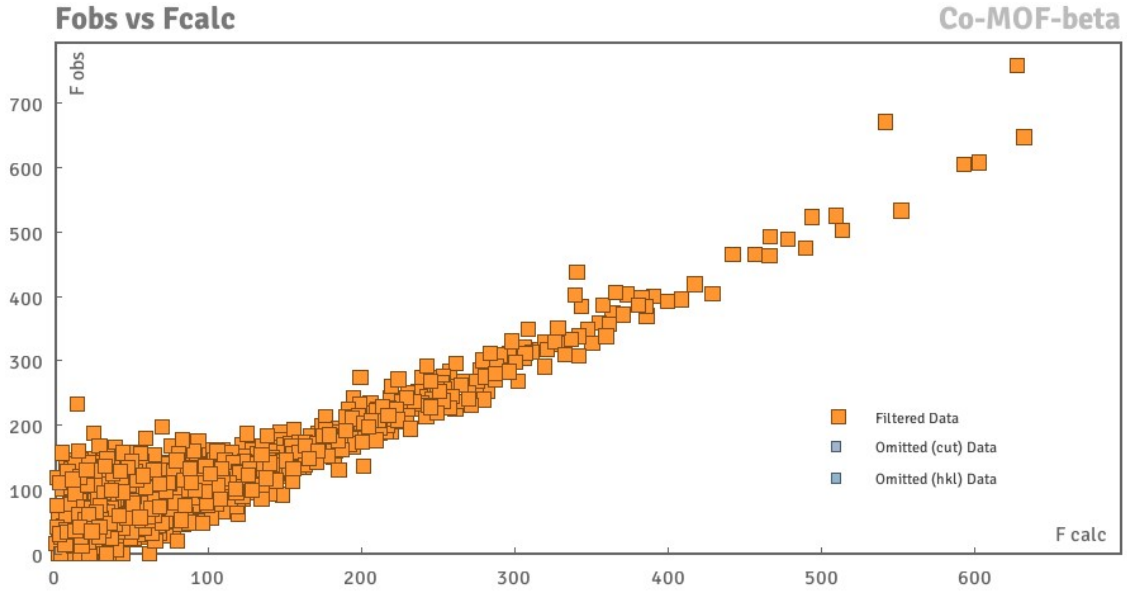

Figure S5. The plot of F_{obs} vs F_{cal} for **Co-MOF-*β***.

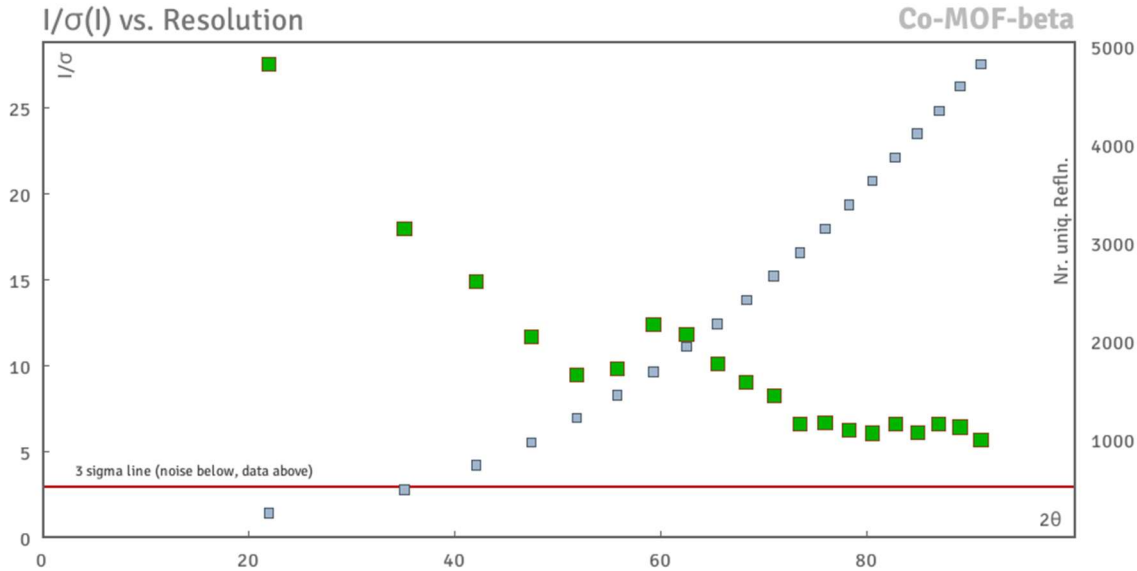

Figure S6. The plot of I / σ(I) vs resolution for **Co-MOF-*β***.

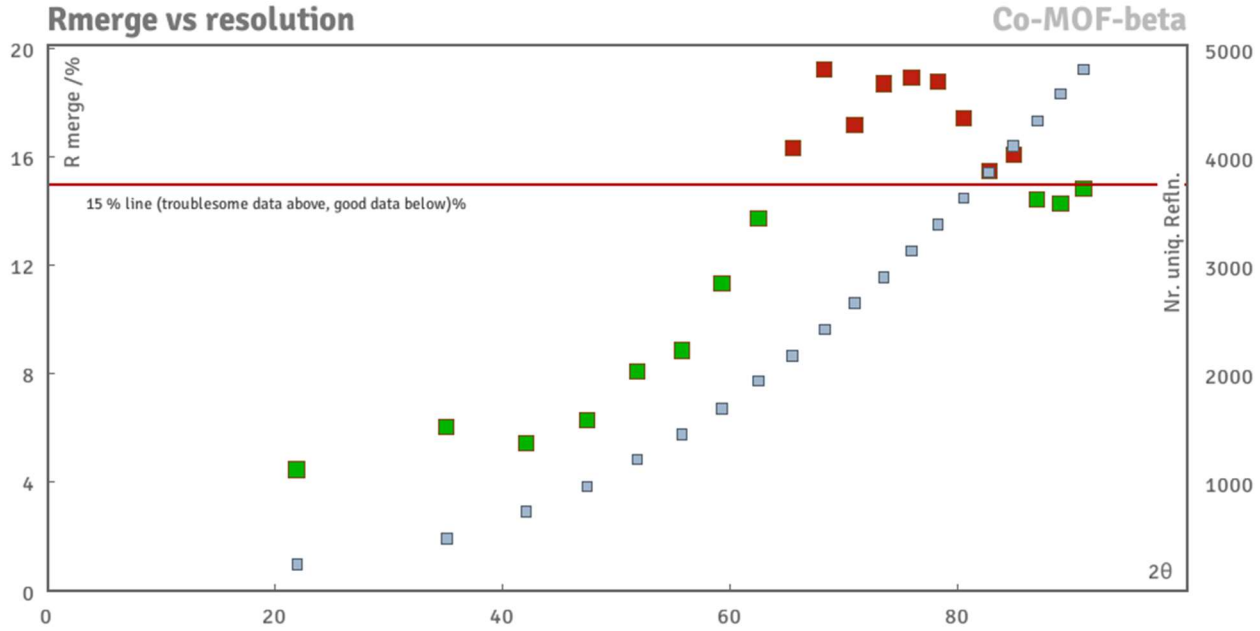

Figure S7. The plot of Rmerge vs resolution for **Co-MOF-*β***.

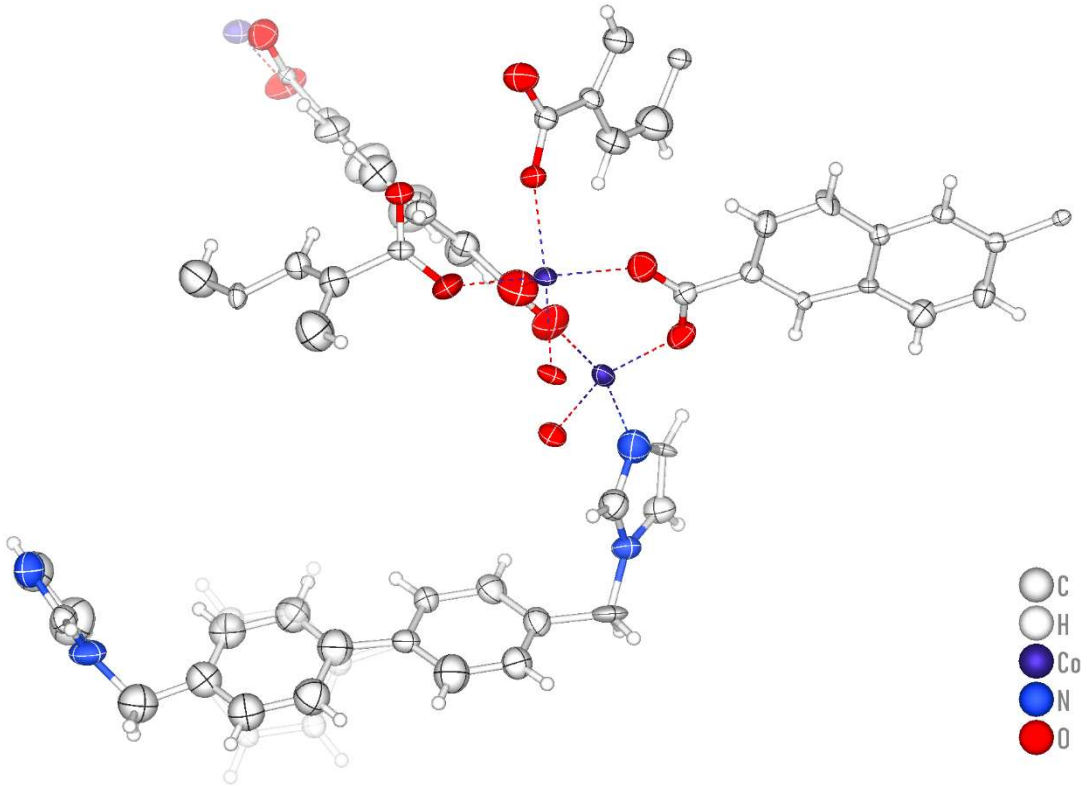

Figure S8. The ORTEP drawing showing thermal ellipsoids at 50% probability for **Co-MOF-*β***.

3. Single-crystal data and structural parameters

Table S1. Crystallographic data and structure refinement summary for **Co-MOF-α** and **Co-MOF-β**.

Compound	**Co-MOF-α**	**Co-MOF-β**
Formula	$C_{65}H_{62}Co_3N_7O_{17.5}$	$C_{56}H_{36}N_4O_{12}Co_3$
Formula weight	1398.02	1133.68
Crystal system	Monoclinic	Monoclinic
Space group	*I*2/*a*	*I*2/*a*
a (Å)	23.078(5)	22.3119(18)
b (Å)	23.525(5)	24.2649(11)
c (Å)	27.050(12)	22.5563(15)
α (°)	90	90
β (°)	106.21(3)	103.654(6)
γ (°)	90	90
V (Å^3)	14102(8)	11866.8(14)
Z	8	8
D_c (g cm cm^{-3})	1.317	1.269
μ (mm^{-1})	0.767	6.984
F(000)	4616	4616
Bond precision	C-C = 0.0104 Å; λ = 0.71073 Å	C-C = 0.0486 Å; λ = 1.54178 Å
Theta range for data collection	3.041 to 25.000°	2.733 to 46.055°
Reflections collected	62790	22003
Independent reflections	12396 [R(int) = 0.1190]	4704 [R(int) = 0.0962]
Data / restraints / parameters	12396 / 398 / 767	4704 / 634 / 731
Completeness / %	99.8%	93.1 %
GOF on F^2	1.048	1.079
R_1 [$I > 2\sigma(I)$]	0.0913	0.2126
wR_2 [$I > 2\sigma(I)$]	0.2501	0.4746
R_1 [all data]	0.1104	0.2276
wR_2 [all data]	0.2649	0.4801
Diff peak, hole (e Å^{-3})	1.643, -0.737	1.484, -0.848
CCDC number	2202608	2202609

$R_1 = \sum||F_o| - |F_c||/\sum|F_o|$, $wR_2 = [\sum w(F_o^2 - F_c^2)^2/\sum w(F_o^2)^2]^{1/2}$

Table S2 Selected bond lengths(Å) and angles(°) for **Co-MOF-α**.

Co(1)-O(1)	2.019(5)	Co(1)-O(2)	2.372(4)
Co(1)-O(5)	1.968(5)	Co(1)-O(7)#1	1.976(5)
Co(1)-N(1)	2.026(6)	Co(2)-O(2)	2.103(4)
Co(2)-O(4)#2	2.062(4)	Co(2)-O(6)	2.065(4)
Co(2)-O(8)#1	2.101(4)	Co(2)-O(10)#2	2.085(4)
Co(2)-O(12)#2	2.072(4)	Co(3)-O(3)	1.930(4)
Co(3)-O(9)	1.962(4)	Co(3)-O(11)	1.968(4)
Co(3)-N(3)#3	2.031(5)		
O(1)-Co(1)-O(2)	57.60(16)	O(5)-Co(1)-O(1)	120.0(2)
O(5)-Co(1)-O(2)	90.96(18)	O(5)-Co(1)-O(7)#1	116.1(2)
O(7)#1-Co(1)-O(1)	115.9(2)	O(7)#1-Co(1)-O(2)	94.04(18)
O(5)-Co(1)-N(1)	105.3(2)	O(7)#1-Co(1)-N(1)	92.6(2)
N(1)-Co(1)-O(1)	100.3(2)	N(1)-Co(1)-O(2)	157.5(2)
O(4)#2-Co(2)-O(2)	177.51(17)	O(4)#2-Co(2)-O(6)	88.7(2)
O(4)#2-Co(2)-O(8)#1	89.04(17)	O(4)#2-Co(2)-O(10)#2	93.90(18)
O(4)#2-Co(2)-O(12)#2	91.80(19)	O(6)-Co(2)-O(2)	89.42(19)
O(6)-Co(2)-O(8)#1	92.83(17)	O(6)-Co(2)-O(10)#2	84.79(17)
O(6)-Co(2)-O(12)#2	179.53(19)	O(8)#1-Co(2)-O(2)	89.47(17)
O(10)#2-Co(2)-O(2)	87.50(19)	O(10)#2-Co(2)-O(8)#1	176.16(18)
O(12)#2-Co(2)-O(2)	90.12(18)	O(12)#2-Co(2)-O(8)#1	87.08(17)
O(12)#2-Co(2)-O(10)#2	95.28(17)	O(3)-Co(3)-O(9)	112.3(2)
O(3)-Co(3)-O(11)	116.9(2)	O(9)-Co(3)-O(11)	120.3(2)
O(3)-Co(3)-N(3)#3	106.7(2)	O(9)-Co(3)-N(3)#3	95.1(2)
O(11)-Co(3)-N(3)#3	101.0(2)		

Symmetry code: #1: x-1/2, -y+1, z; #2: -x+1, y+1/2, -z-1/2; #3: x+1/2, -y, z.

Table S3 Selected bond lengths(Å) and angles(°) for **Co-MOF-*β***.

Co(1)-O(1)	1.98(2)	Co(1)-O(5)	1.97(2)
Co(1)-O(7)	2.00(2)	Co(1)-N(1)	2.05(3)
Co(2)-O(2)	2.15(3)	Co(2)-O(4)#1	2.07(2)
Co(2)-O(6)	2.08(2)	Co(2)-O(8)	2.07(2)
Co(2)-O(10)	2.10(2)	Co(2)-O(12)	2.10(3)
Co(3)-O(3)	1.96(2)	Co(3)-O(9)#2	2.05(2)
Co(3)-O(10)#2	2.37(2)	Co(3)-O(11)#2	1.97(2)
Co(3)-N(3)#3	2.02(3)		
O(1)-Co(1)-O(7)	114.4(10)	O(5)-Co(1)-O(1)	117.2(11)
O(5)-Co(1)-O(7)	117.8(9)	O(1)-Co(1)-N(1)	100.4(13)
O(5)-Co(1)-N(1)	106.8(11)	O(7)-Co(1)-N(1)	95.3(11)
O(4)#1-Co(2)-O(2)	178.5(10)	O(4)#1-Co(2)-O(6)	86.4(9)
O(4)#1-Co(2)-O(8)	88.1(9)	O(4)#1-Co(2)-O(10)	93.1(9)
O(4)#1-Co(2)-O(12)	92.8(11)	O(6)-Co(2)-O(2)	92.6(10)
O(6)-Co(2)-O(10)	89.2(9)	O(6)-Co(2)-O(12)	179.1(11)
O(8)-Co(2)-O(2)	93.1(10)	O(8)-Co(2)-O(6)	93.8(9)
O(8)-Co(2)-O(10)	176.8(9)	O(8)-Co(2)-O(12)	85.8(9)
O(10)-Co(2)-O(2)	85.7(10)	O(12)-Co(2)-O(2)	88.2(11)
O(12)-Co(2)-O(10)	91.2(9)	O(3)-Co(3)-O(9)#2	118.4(11)
O(3)-Co(3)-O(10)#2	100.7(9)	O(3)-Co(3)-O(11)#2	112.6(11)
O(9)#2-Co(3)-O(10)#2	58.4(8)	O(11)#2-Co(3)-O(9)#2	122.4(10)
O(11)#2-Co(3)-O(10)#2	88.3(8)	O(3)-Co(3)-N(3)#3	98.6(12)
O(11)#2-Co(3)-N(3)#3	101.9(11)	N(3)#3-Co(3)-O(9)#2	95.3(12)
N(3)#3-Co(3)-O(10)#2	152.7(11)		

Symmetry codes: #1: -x+0, y+1/2, -z-1/2; #2: -x+0, y-1/2, -z-1/2; #3: x+1/2, -y, z.

4. Additional structure figures

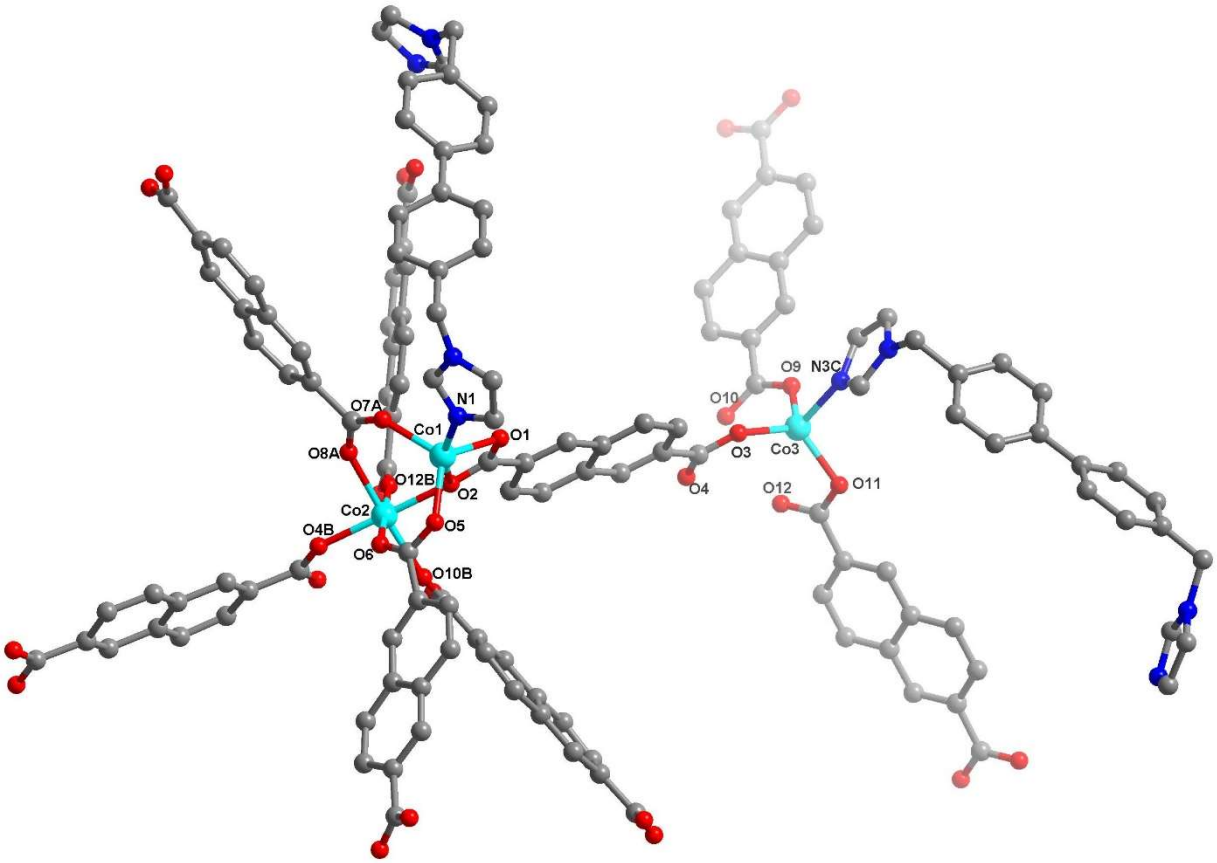

Figure S9. The coordination environment of the cobalt ions in **Co-MOF-α**. Symmetric codes: A: *x*-1/2, -*y*+1, *z*; B: -*x*+1, *y*+1/2, -*z*+1/2; C: *x*+1/2, -*y*, *z*. One-fold disorder of ndc^{2-} ligands is shown for clarity.

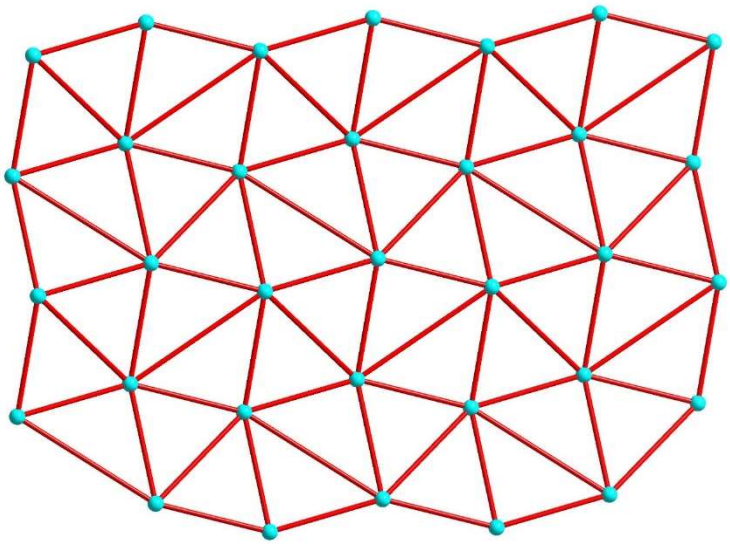

Figure S10. The 6-connected hxl/Shubnikov plane net (3,6) with $\{3^6.4^6.5^3\}$ topology in **Co-MOF-α** when the trinuclear $[Co_3(COO)_6]$ units as 6-connected secondary building units (SBUs).

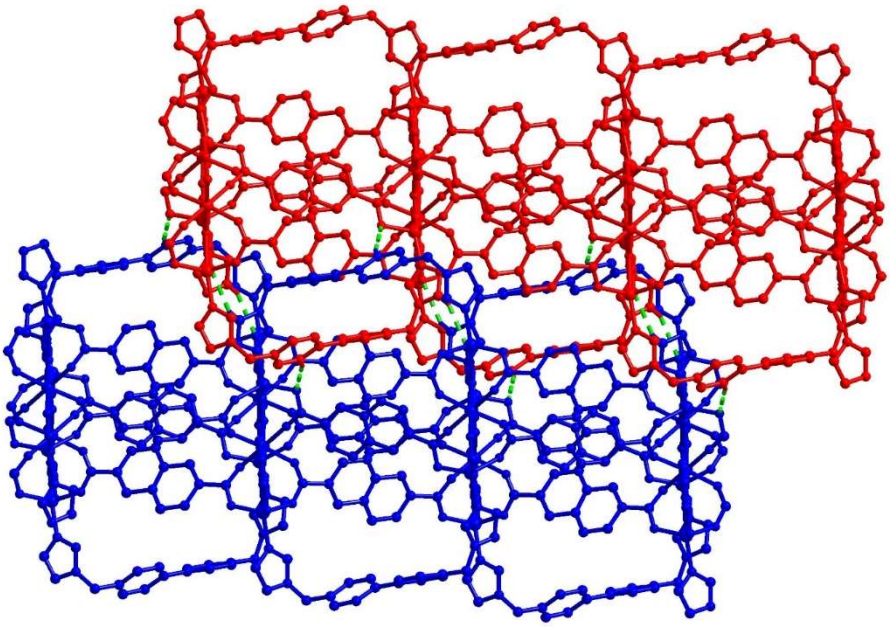

Figure S11. The C–H···O weak interactions (showing in green dash line) among 2D layers in **Co-MOF-α**. One-fold disorder of ndc^{2-} ligands is shown for clarity.

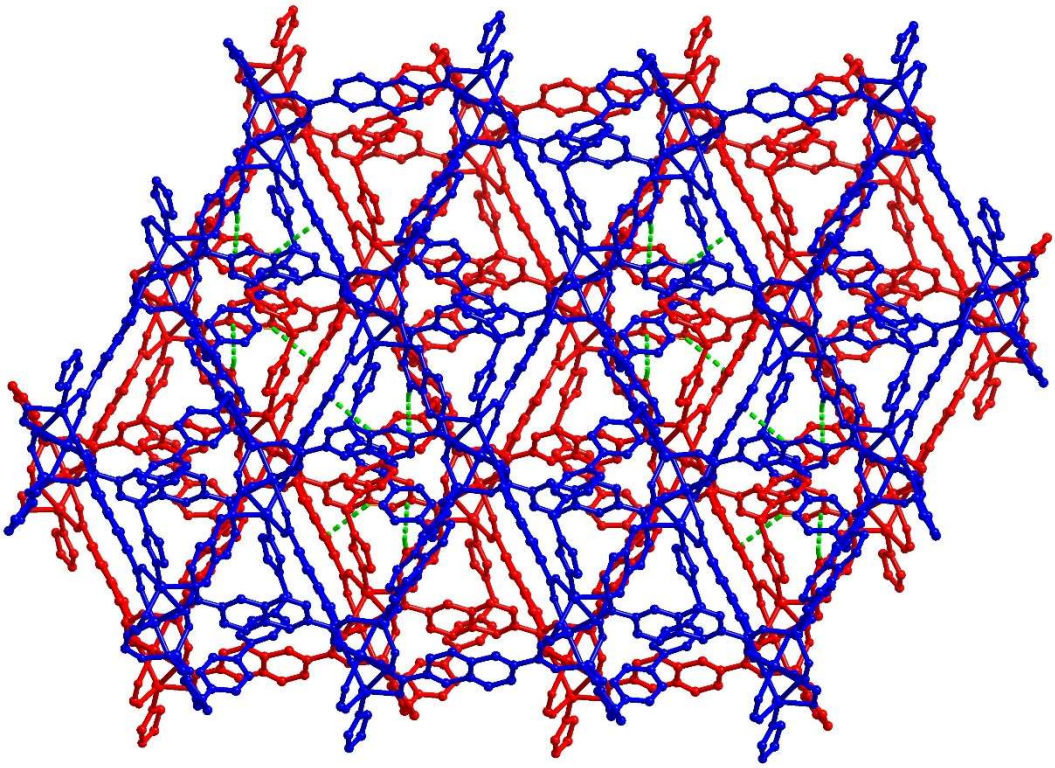

Figure S12. The C–H···π interactions (showing in green dash line) between adjacent 2D layers in **Co-MOF-α**. One-fold disorder of ndc^{2-} ligands is shown for clarity.

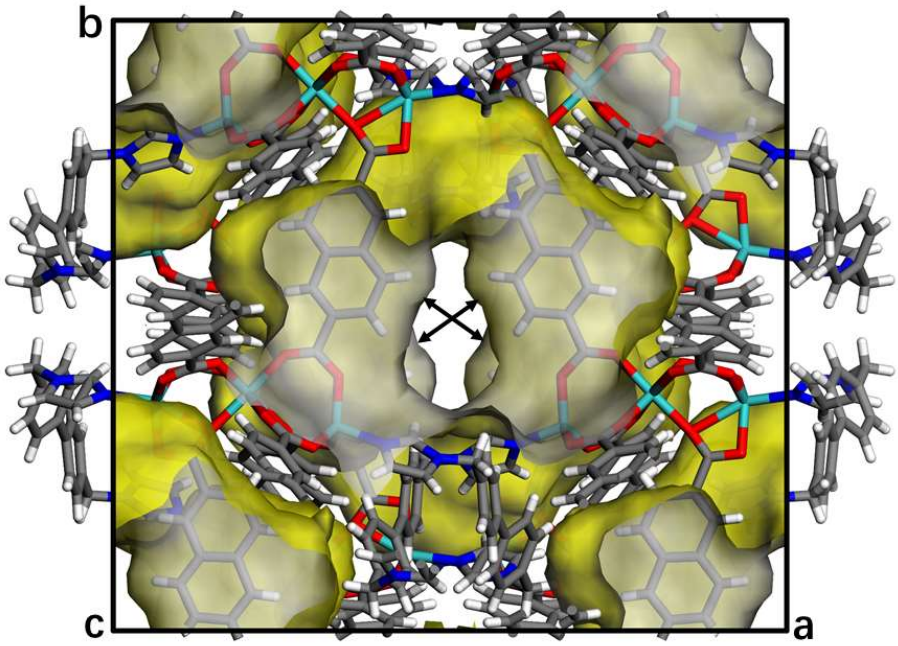

Figure S13. Illustrations of the position of pore diameters (approximately 3.3 Å) viewed along the *c*-axis for **Co-MOF-α**. One-fold disorder of ndc^{2-} ligands is shown for clarity.

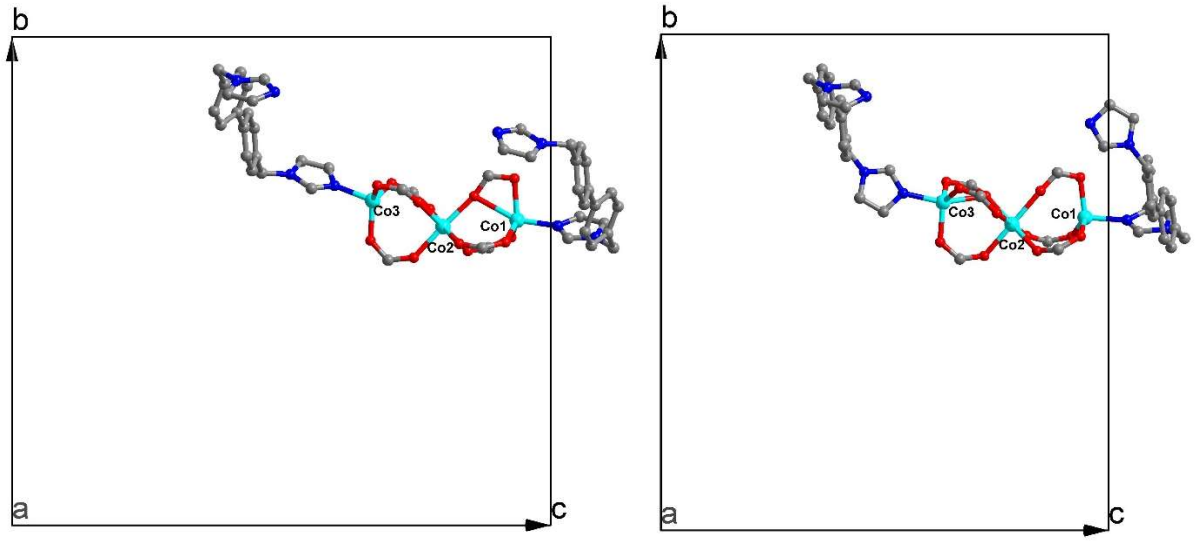

Figure S14. The comparison diagrams of the trinuclear SBU for **Co-MOF-α** (left) and **Co-MOF-β** (right) viewed along the *a*-axis. In **Co-MOF-α** (left), the coordination modes of Co1 and Co2 are trigonal bipyramidal and tetrahedral geometries, respectively. After removal of guests, the coordination modes of Co1 (trigonal bipyramidal) transformed to tetrahedral geometry because one Co-O bond (Co1-O2) in **Co-MOF-α** broke off. Meanwhile, the coordination modes of Co3 (tetrahedral) transformed to trigonal bipyramidal geometry because one new Co3-O bond formed when the structure transformed to **Co-MOF-β**.

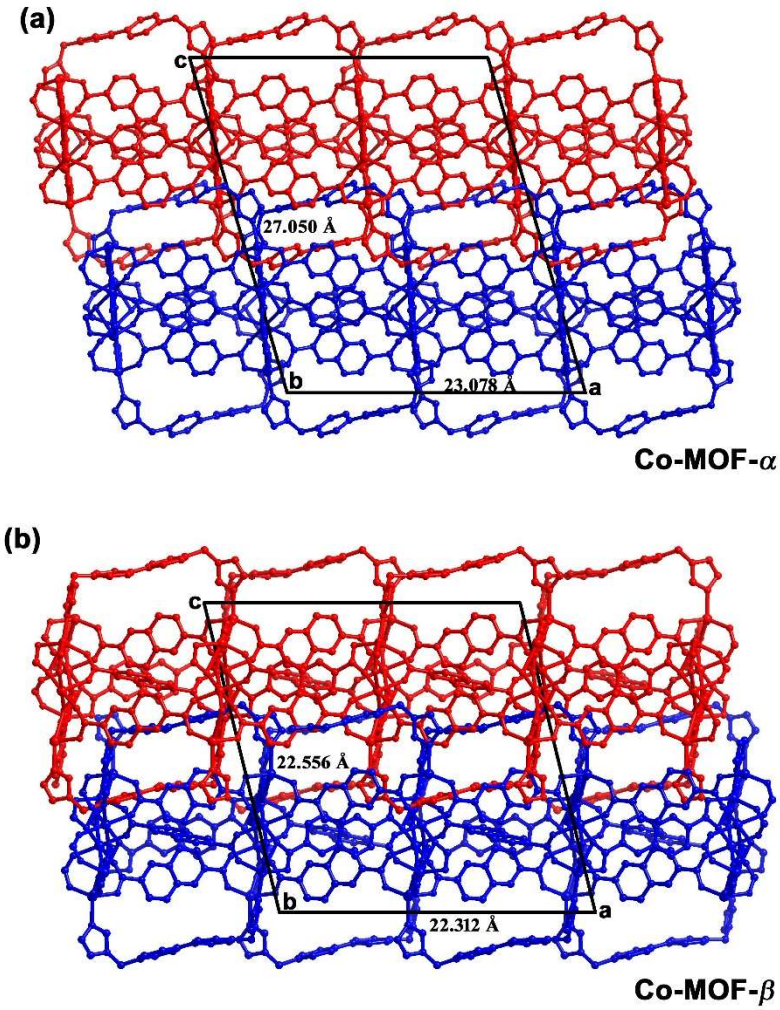

Figure S15. The packing diagram viewed along the *b*-axis showing the structural transformations between **Co-MOF-*α*** and **Co-MOF-*β***. One-fold disorder of ndc^{2-} and bimb ligands is shown for clarity.

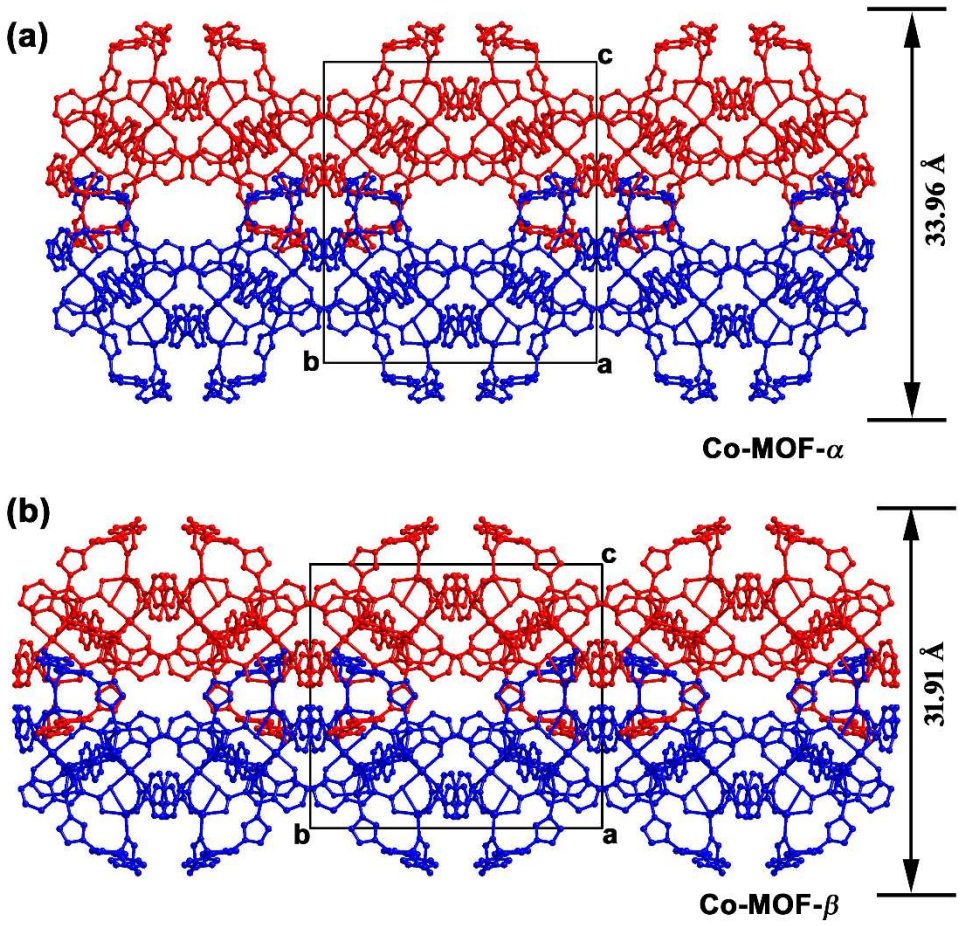

Figure S16. The packing diagram viewed along the *a*-axis showing the structural transformations between **Co-MOF-*α*** and **Co-MOF-*β***. One-fold disorder of ndc^{2-} and bimb ligands is shown for clarity.

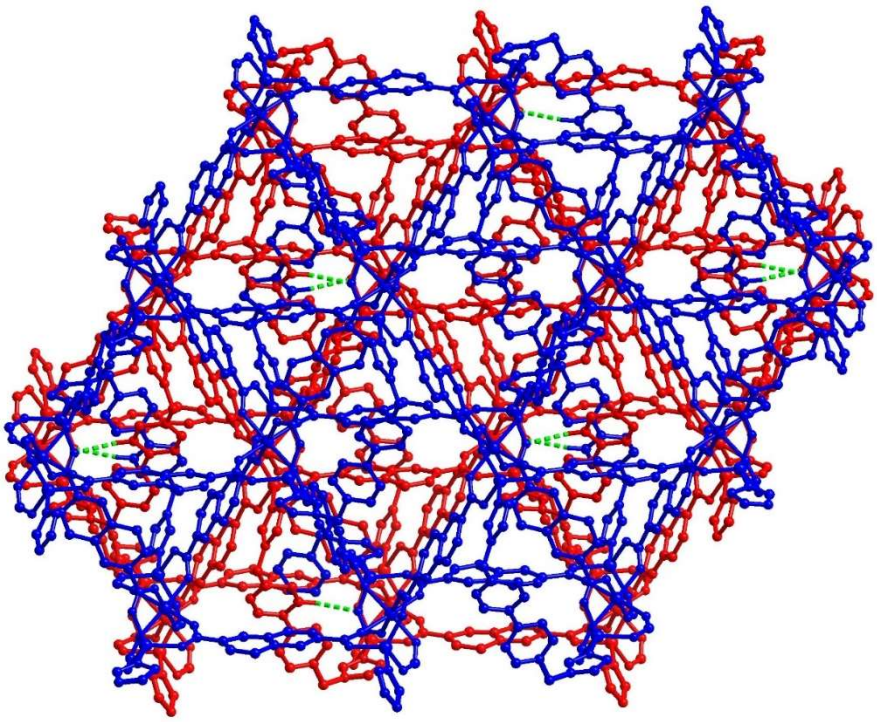

Figure S17. The intramolecular C–H···O weak interactions (showing in green dash line) among 2D layers in **Co-MOF-*β***. One-fold disorder of bimb ligands is shown for clarity.

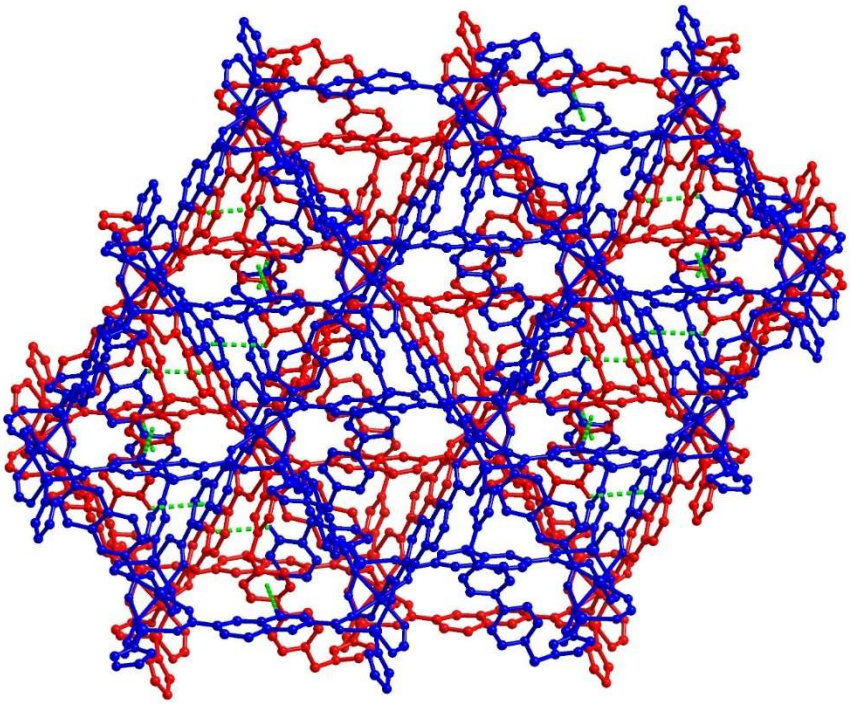

Figure S18. The C–H···π interactions (showing in purple dash line) between adjacent 2D layers in **Co-MOF-*β***. One-fold disorder of bimb ligands is shown for clarity.

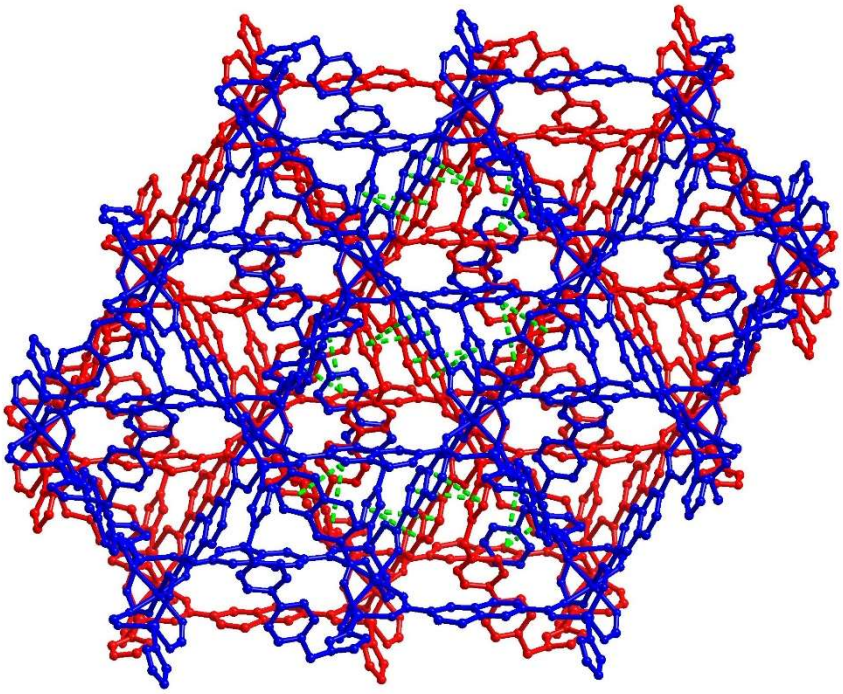

Figure S19. The π-π interactions (showing in purple dash line) between adjacent 2D layers in **Co-MOF-*β***. One-fold disorder of bimb ligands is shown for clarity.

5. Summary tables of structural differences between Co-MOF-α and Co-MOF-β.

Table S4. Comparative analysis of structural differences between **Co-MOF-α** and **Co-MOF-β**.

Compounds	**Co-MOF-α**	**Co-MOF-β**
Coordination geometry of Co^{2+} ions	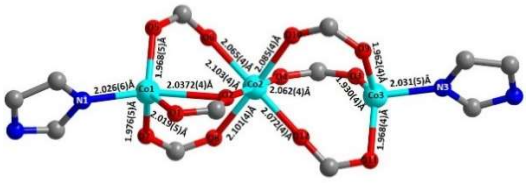 Co–O: 1.930(4)-2.372(4) Å Co–N: 2.026(6)/2.031(5) Å ∠O–Co–O: 57.60(16)º-179.53(19)º ∠O–Co–N: 92.6(2)º-157.5(2)º	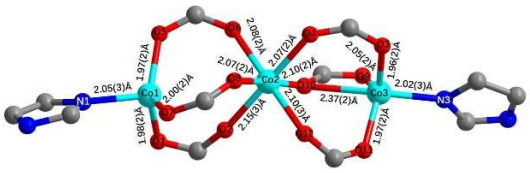 Co–O: 1.96(2)-2.37(2) Å Co–N: 2.02(3)/2.05(3) Å ∠O–Co–O: 58.4(8)º-179.1(11)º ∠O–Co–N: 95.3(11)º-152.7(11)º
Coordination modes of ndc^{2-} ligands (one-fold disorder of ndc^{2-} ligands is shown for clarity in **Co-MOF-α**)	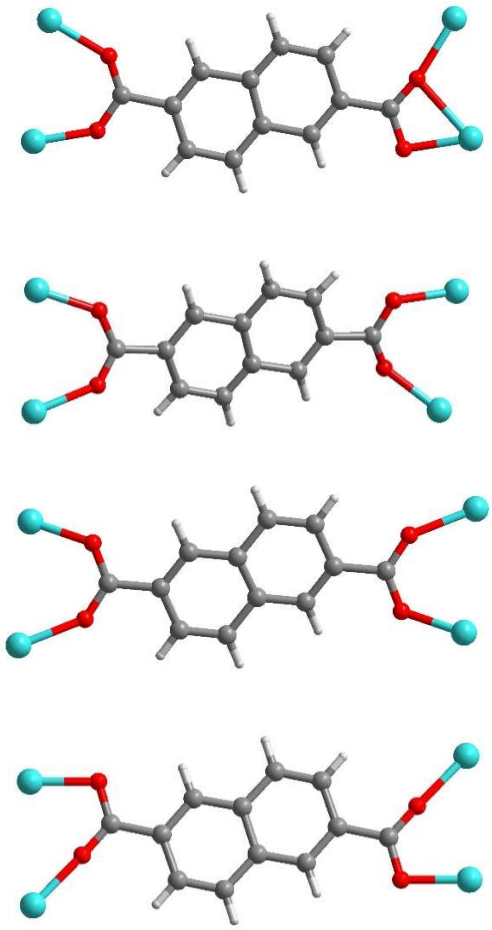	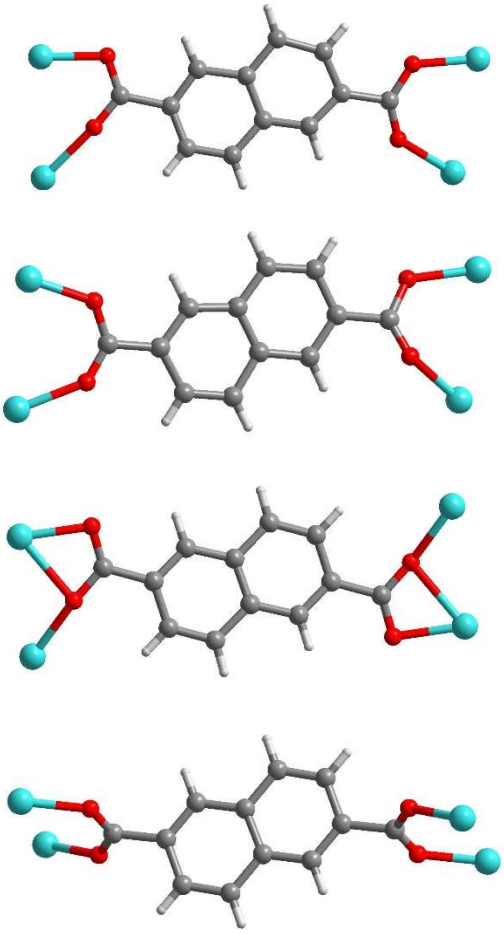
Geometry parameters between the cobalt ion and carboxylate plane		

	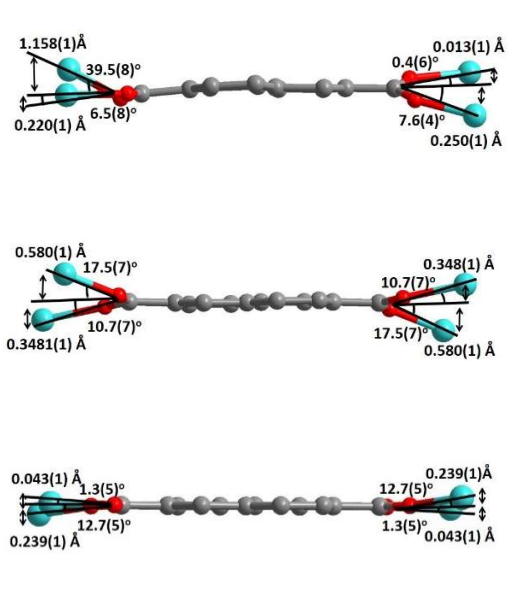	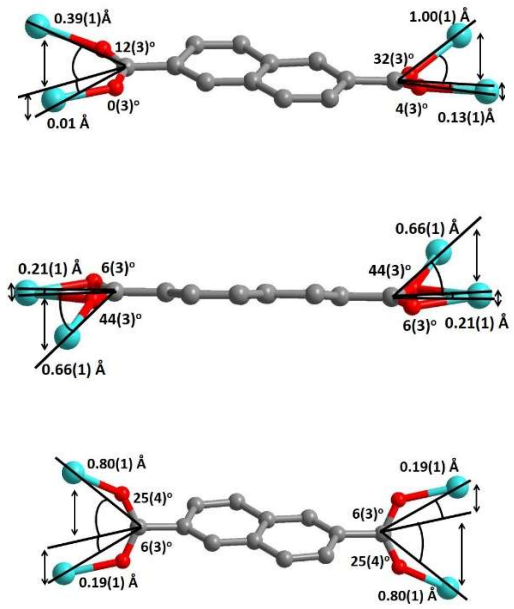
dihedral angles between benzene rings, imdazole and nearby benzene rings	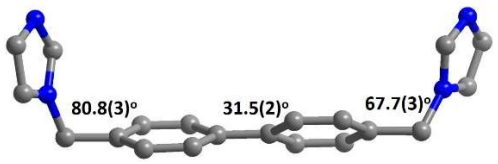	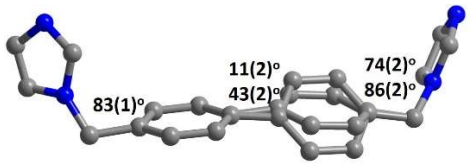
The nearby Zn⋯Zn distance in the $[Zn_2(3\text{-tba})_2]$ ring	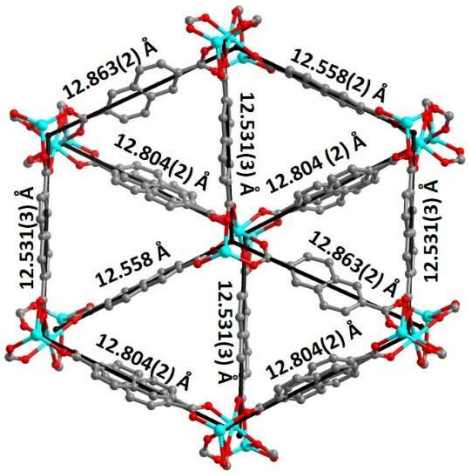	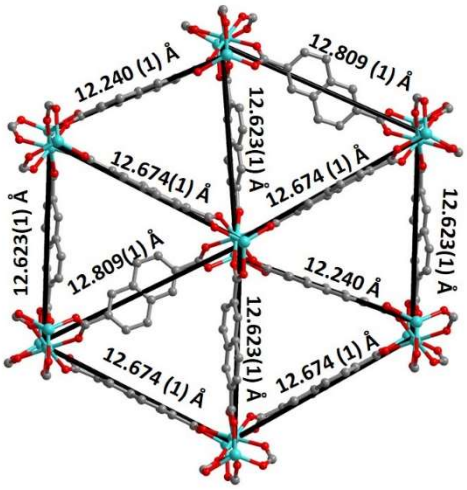

6. Summary tables of weak interactions in the Co-MOF-α and Co-MOF-β.

Table S5. Possible intermolecular, hydrogen bonds (Å, º) in **Co-MOF-α** and **Co-MOF-β**.

	D–H	H···A	D···A	∠D–H···A
Co-MOF-α				
C(43)–H(43)···O(11a)	0.93	2.49	3.382(9)	161
C(56)–H(56)···O(1b)	0.93	2.59	3.385(11)	144
Co-MOF-β				
C(45)–H(45)···O(11c)	0.93	2.49	3.290(3)	144

Symmetry code: (a) -*x*+1, -*y*, -*z*; (b) -*x*+1/2, y, -*z*; (c) *x*, -*y*+1/2, *z*+1/2.

Table S6. Analysis of shortest aromatic π-π stacking interaction (Å) in **Co-MOF-β**.

	distance between ring centroids	distance between ring centroid to plane	distance between ring centroid to plane
Co-MOF-α			
$Ring_{(N1,C37,N2,C39,C38)}$–$Ring_{(C17B,C18B,C19B,C20B,C21B,C22B)}$[a]	3.876(7)	3.155(4)	3.690(6)
Co-MOF-β			
$Ring_{(N1,C37,N2,C39,C38)}$–$Ring_{(C14,C15,C16,C17,C22,C23)}$[b]	3.84(2)	3.40(2)	3.51(1)
$Ring_{(N1,C37,N2,C39,C38)}$–$Ring_{(C17,C18,C24,C20,C21,C22)}$[b]	3.50(2)	3.35(1)	3.41(2)
$Ring_{(C32,C33,C34,C34\_c,C35\_c,C36)}$–$Ring_{(C47A,C48A,C49A,C50A,C51A,C52A)}$[d]	3.94(3)	3.53(3)	3.82(2)
$Ring_{(C32,C33,C34,C34\_c,C35\_c,C36)}$–$Ring_{(C47A,C48A,C49A,C50A,C51A,C52A)}$[e]	3.98(3)	3.37(2)	3.54(3)
$Ring_{(C32,C33,C34,C34\_c,C35\_c,C36)}$–$Ring_{(C47B,C48B,C49B,C50B,C51B,C52B)}$[d]	3.87(3)	2.96(2)	3.48(3)
$Ring_{(C34,C35,C36\_c,C32\_c,C33\_g,C34\_c)}$–$Ring_{(C47A,C48A,C49A,C50A,C51A,C52A)}$[d]	3.98(3)	3.37(2)	3.54(3)
$Ring_{(C34,C35,C36\_c,C32\_c,C33\_c,C34\_c)}$–$Ring_{(C47A,C48A,C49A,C50A,C51A,C52A)}$[e]	3.95(3)	3.53(3)	3.82(2)
$Ring_{(C34,C35,C36\_c,C32\_c,C33\_c,C34\_c)}$–$Ring_{(C47B,C48B,C49B,C50B,C51B,C52B)}$[e]	3.87(3)	2.96(2)	3.48(3)

Symmetry code: (a) -*x*+3/2, *y*, -*z*; (b) -*x*+1/2, y, -*z*; (c) –*x*-1/2, -*y*+1/2, -*z*-1/2; (d) –*x*-1/2, *y*, -*z*; (e) *x*, -y+1/2, *z*-1/2.

Table S7. Possible C–H···π interactions (Å,º) in **Co-MOF-α** and **Co-MOF-β**.

	H···Cg	C···Cg	∠C–H···Cg
Co-MOF-α			
C(34)–H(34)···$Ring_{(C47,C48,C49,C50,C51,C52)}$[a]	2.68	3.602(6)	169
C(52)–H(52)···$Ring_{(C17B,C18B,C19B,C20B,C21B,C22B)}$[b]	2.91	3.742(10)	150
Co-MOF-β			
C(4)–H(4)···$Ring_{(C41,C42,C43,C44,C45,C46)}$[c]	2.75	3.66(4)	166
C(51A)–H(51A)···$Ring_{(C17,C18,C24,C20,C21,C22)}$[d]	2.78	3.46(5)	131
C(52A)–H(52A)···$Ring_{(C17,C18,C24,C20,C21,C22)}$[d]	2.99	3.57(4)	122

Symmetry code: (a) *x*+1/2, *y*-1/2, *z*-1/2; (b) -*x*+1, -y+1, -*z*; (c) *x*, -*y*+1/2, *z*-1/2; (d) -*x*, -*y*+1,-*z*.

7. Powder X-ray diffraction (PXRD)

Powder X-ray diffraction (PXRD) patterns were recorded at the room temperature on a Rigaku MiniFlex600 X-ray diffractometer (40 kV, 15 mA) with Cu-Kα (λ = 1.5405 Å) radiation in a 2theta range from 3 to 40°. All the calculated PXRD patterns are simulated from single-crystal diffraction by using Mercury v3.8 software (Cambridge Crystallographic Data Centre, Cambridge, UK).

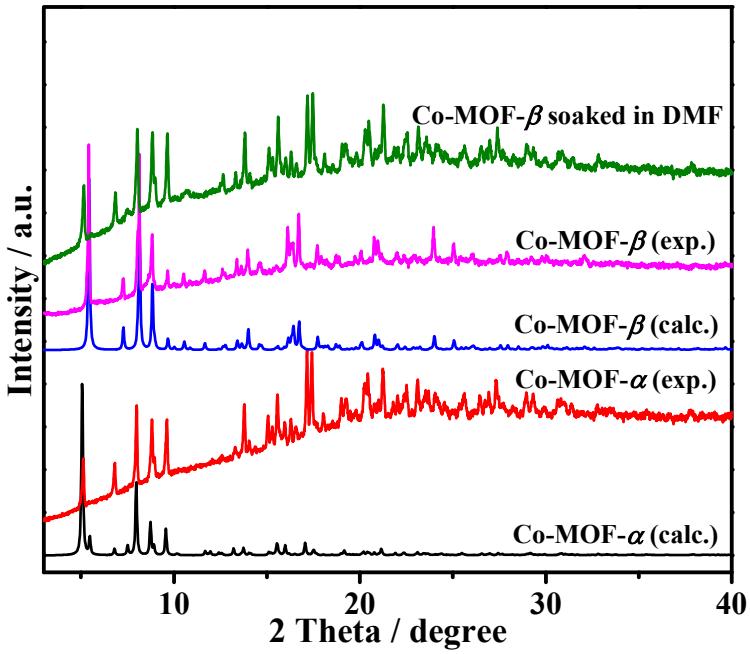

Figure S20. PXRD patterns of **Co-MOF-α**, **Co-MOF-β**, and **Co-MOF-β** after soaking in DMF for 24 h.

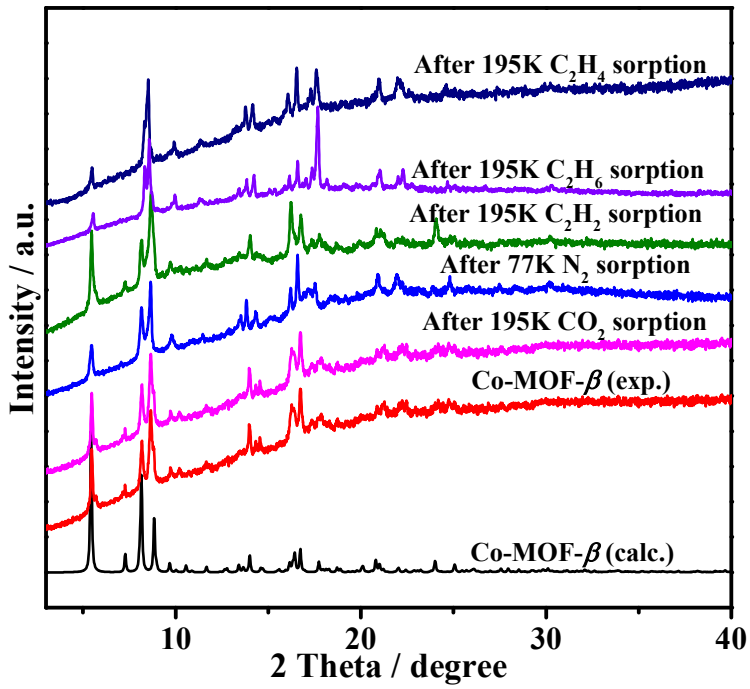

Figure S21. PXRD patterns of **Co-MOF-β** under different conditions.

8. Thermogravimetric analysis (TGA)

Thermogravimetric analysis (TGA) performed using a Netzsch STA 449C instrument with a heating rate of 10.0 °C/min from the room temperature to 650 ºC under N_2 atmosphere.

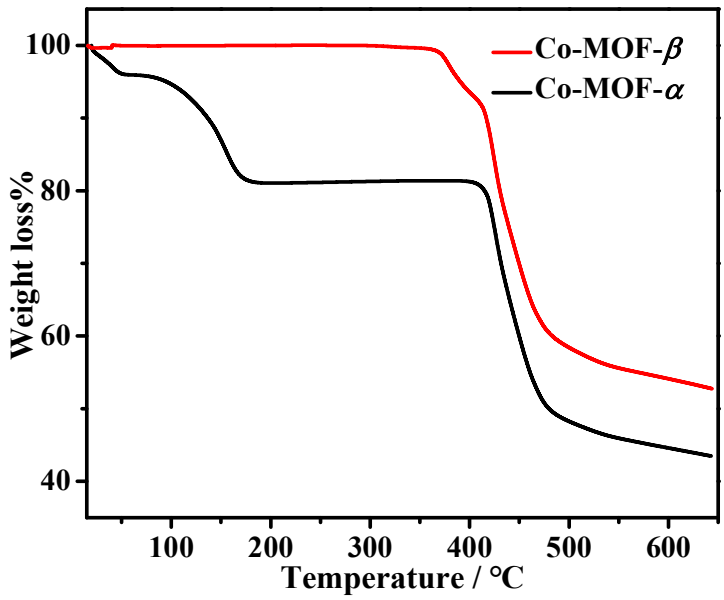

Figure S22. TG curves of **Co-MOF-*α*** and **Co-MOF-*β*** in a N_2 environment. The TGA urve of **Co-MOF-*α*** displays a weight loss of 18.96% at 200 °C, resulting from the release of three molecules of DMF and 2.5 H_2O molecules per formula unit (calc. 18.91%).

9. IR spectra

Infrared spectra were recorded from KBr pellets on a Thermo Scientific Nicolet IS 10 FTIR spectrometer in the range of 400-4000 cm^{-1}.

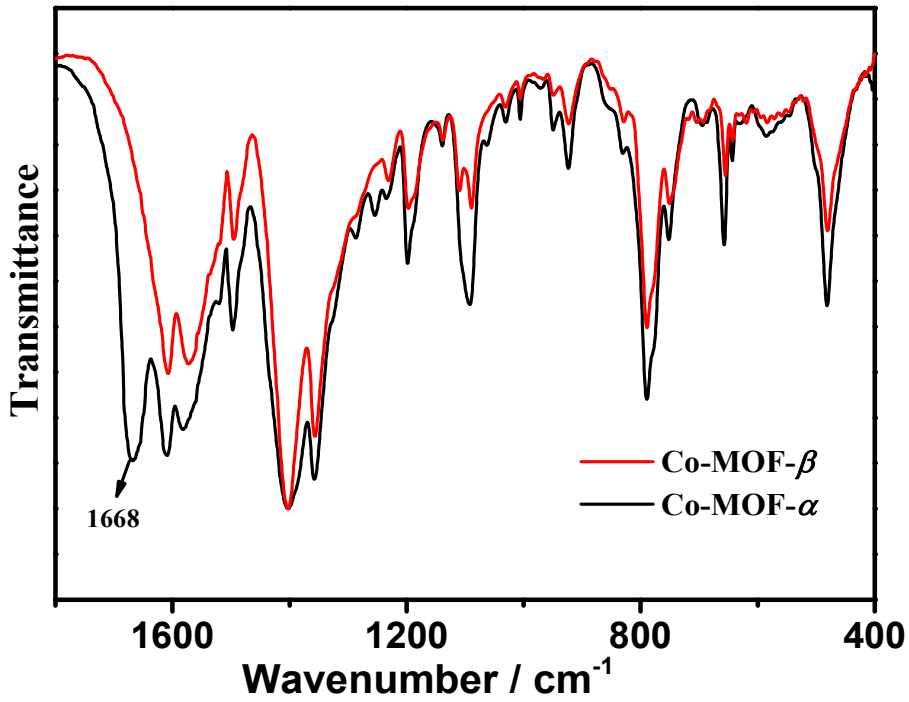

Figure S23. IR spectra of **Co-MOF-*α*** and **Co-MOF-*β***. The lack of C=O stretching peaks at about 1668 cm^{-1} in the IR spectra of **Co-MOF-*β*** confirms the full release of DMF guests.

10. Raman Spectra

The Raman spectra were acquired with High-resolution Raman imaging spectrometer (HORIBA Jobin Yvon, LabRAM Odyssey, France). The wave number was collected in the rang of 1250~1700 cm^{-1}. The spectra were collected by point mapping (785 nm excitation laser, laser power 10 mW, acquisition time 10 secs, 2 accumulations).

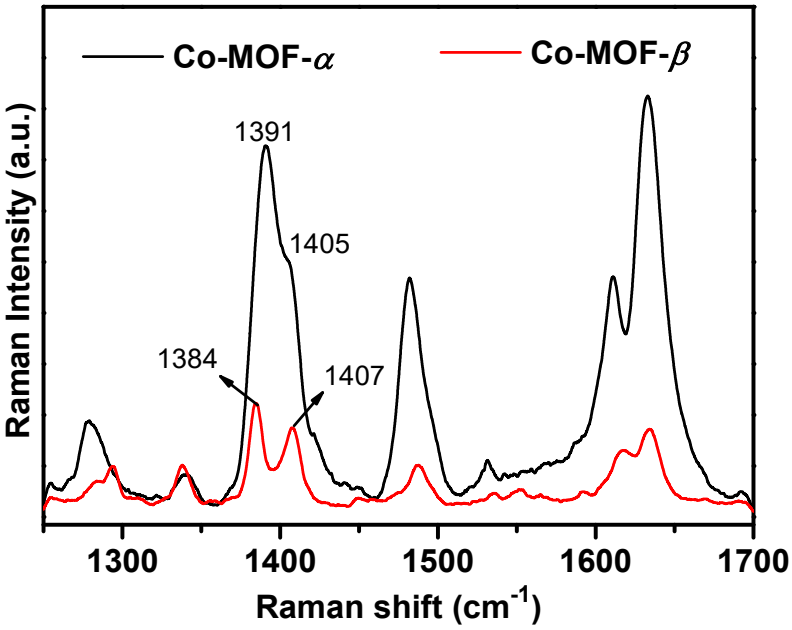

Figure S24. Raman spectra of **Co-MOF-*α*** and **Co-MOF-*β***. Raman spectra of **Co-MOF-*α*** indicate that the band with one peak at 1391 cm^{-1} with a shoulder peak at 1405 cm^{-1} corresponds to $\nu_{sym}(COO^-)$ vibration, whereas the $\nu_{sym}(COO^-)$ vibration of **Co-MOF-*β*** exhibits two obvious peaks at 1384 cm^{-1} and 1407 cm^{-1}. Moreover, the peak 1384 cm^{-1} for **Co-MOF-*β*** show a slight shift (~7 cm^{-1}) in contrast to that of **Co-MOF-*α***. These differences are consistent with the respective coordination environments of carboxylate groups.

11. Gas adsorption measurements

All the adsorption isotherms were measured by using Belsorp-max gas adsorption instrument (MicrotracBEL Corp from Japan), respectively. Before gas sorption experiment, the samples of **Co-MOF-*β*** was was placed in the quartz tube and degased under the room temperature for 12 hrs prior to measurements. All the adsorption isotherms were tested by using relative pressure mode. P_0 is the saturation pressure, and the value is 80.735 kPa in Kunming (a plateau area with an altitude of about 1950 m), China.

12. The calculation of Langmuir surface area

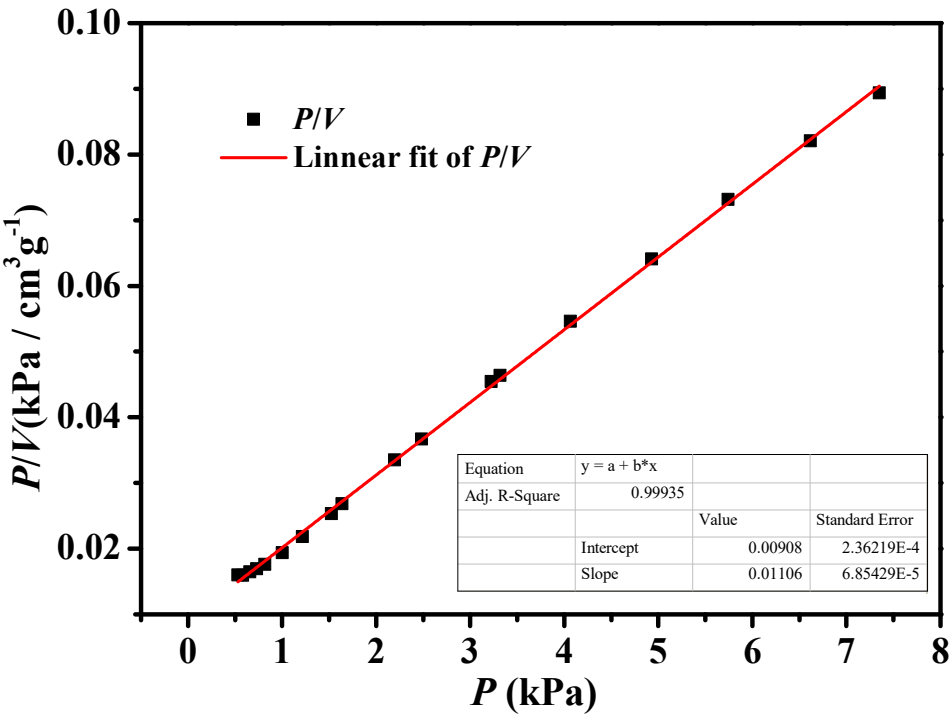

Figure S25. Langmuir plot for the CO_2 adsorption isotherm of **Co-MOF-*β*** at 195 K, and the range *P* from 0.5291 to 7.3509 kPa satisfies for applying the Langmuir theory.

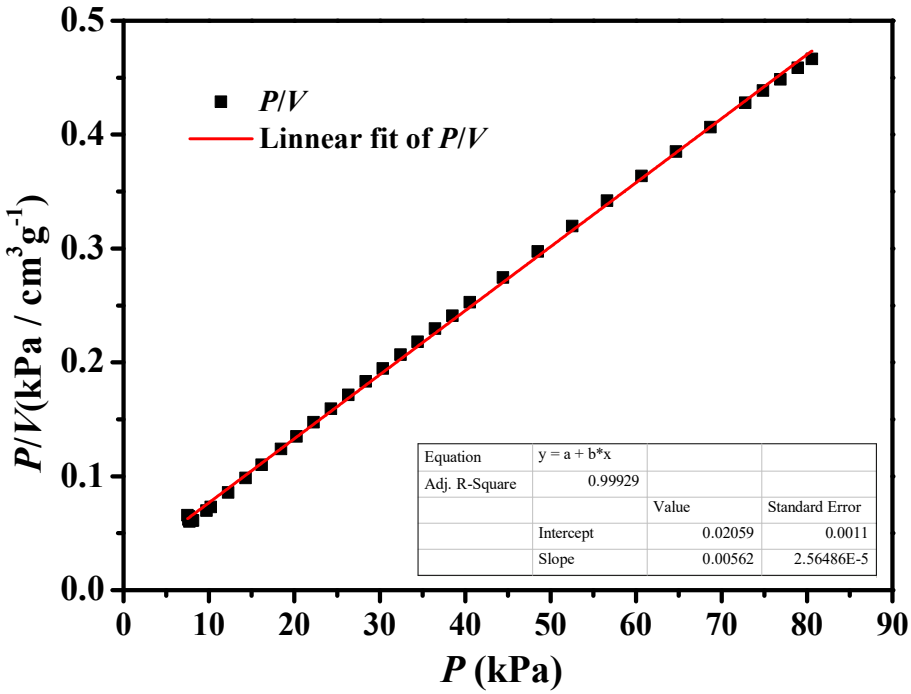

Figure S26. Langmuir plot for the CO_2 adsorption isotherm of **Co-MOF-*β*** at 195 K, and the range *P* from 7.4921 to 80.568 kPa satisfies for applying the Langmuir theory.

The adsorption isotherms were converted into plots of P/V vs. P for determining the appropriate range. As shown in Fig. S13-Fig. S14, the range P from 0.5291 to 7.3509 kPa and the range P from 7.4921 to 80.568 kPa satisfy for applying the Langmuir theory. After having identified the appropriate low pressure Langmuir P range, the analysis proceeds according to the standard method via the linearized Langmuir equation.

$$P/V = P/V_m + 1/BV_m$$

from which the parameters V_m is obtained from the relation $V_m = 1/s$, s being the slope with the ordinate of the plot P/V vs. P. The surface area is then obtained from $A_{Langmuir} = V_m \sigma_m N_A$ with σ_m being the cross-sectional area of CO_2 at liquid density (1.037×10^{-26} m^2), and N_A is the Avogadro´s number.

13. The calculation of BET surface area

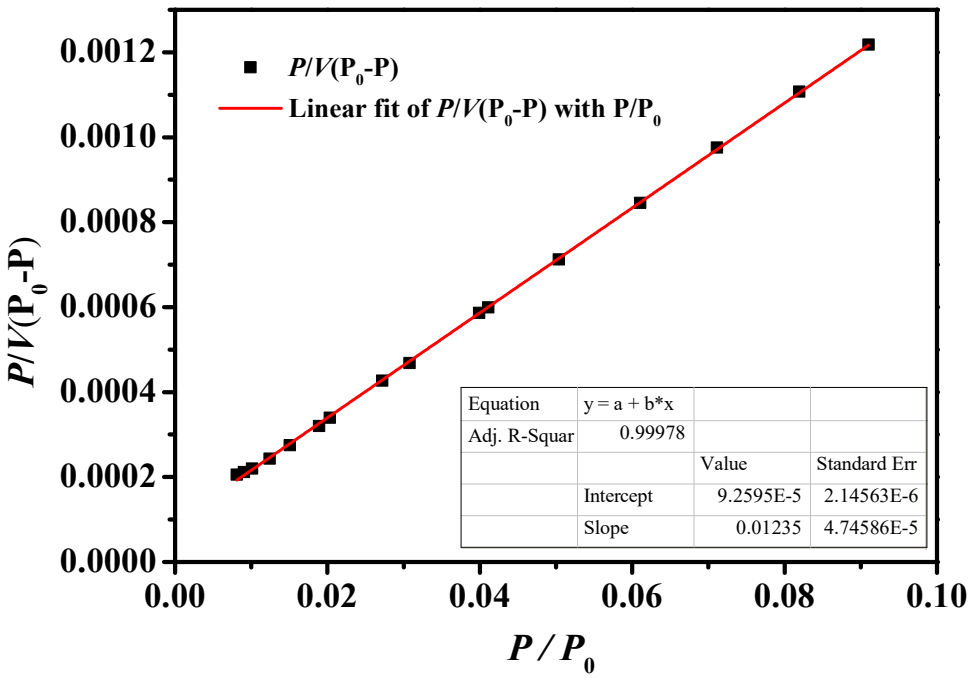

Figure S27. BET plot for the CO_2 adsorption isotherm of **Co-MOF-*β*** at 195 K, and the range P/P_0 from 0.0081 to 0.091 kPa satisfies for applying the BET theory.

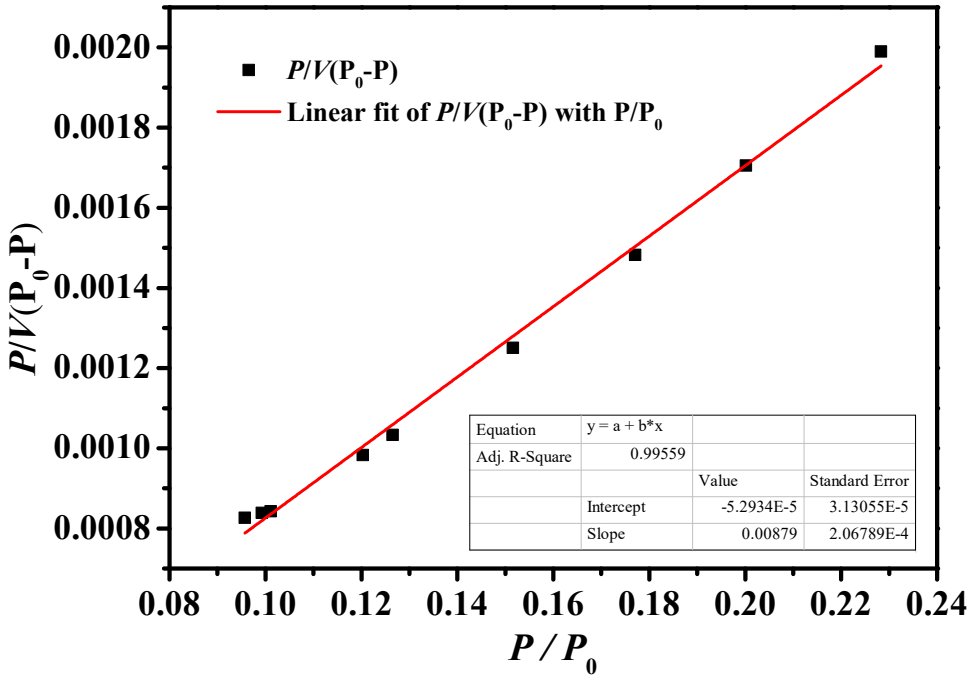

Figure S28. BET plot for the CO_2 adsorption isotherm of **Co-MOF-*β*** at 195 K, and the range P/P_0 from 0.0928 to 0.4768 kPa satisfies for applying the BET theory.

The adsorption isotherms were converted into plots of $1/[V(P_0/P - 1)]$ vs. P/P_0 for determining the appropriate range. As shown in Fig. S15 and Fig. S16, the range P/P_0 from 0.0081 to 0.091 kPa and the range P/P_0 from 0.0928 to 0.4768 kPa satisfy for applying the BET theory. After having identified the appropriate low pressure BET P/P_0 range, the analysis proceeds according to the standard method via the linearized BET equation.

$$\frac{P}{V(P_0 - P)} = \frac{1}{V_m c} + \frac{(C-1)}{V_m c}\frac{P}{P_0}$$

from which the BET parameters c is obtained from the relation $c = s/i + 1$, s being the slope and i being the intercept with the ordinate of the plot $1/[V(P_0/P - 1)]$ vs. P/P_0. The parameter V_m is then given by $V_m = 1/(s + i)$. The surface area is then obtained from $A_{BET} = V_m \sigma_m N_A$ with σ_m being the cross-sectional area of CO_2 at liquid density (1.037×10^{-26} m^2), and N_A is the Avogadro´s number.

14. Calculation of enthalpy of adsorption (Q_{st}) for C_2H_2, C_2H_4, C_2H_6, CO_2, CH_4

$$\ln P = \ln N + \sum_{i=0}^{m} a_i N^i + \sum_{i=0}^{n} \binom{n}{k} b_i N^i$$

$$Q_{st} = -R \sum_{i=0}^{m} a_i N^i$$

A virial-type expression of the above form was used to fit the combined isotherm data of C_2H_2 for **Co-MOF-β** at 273, 283 and 298 K, where P is the pressure described in Pa, N is the adsorbed amount in mmol/g, T is the temperature in K, a_i and b_i are virial coefficients, and m and n are the number of coefficients used to describe the isotherms. Q_{st} is the coverage-dependent enthalpy of adsorption and R is the universal gas constant.

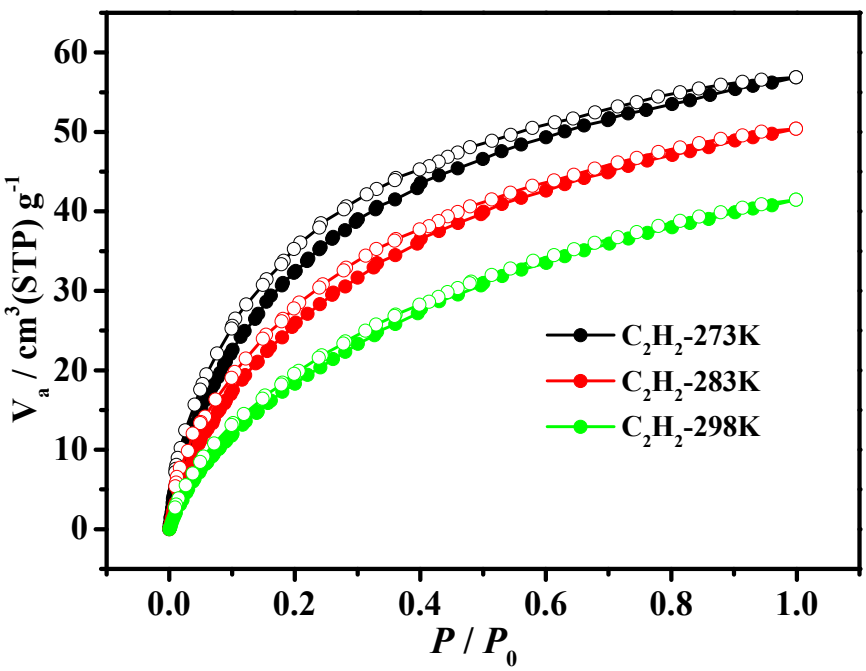

Figure S29. C_2H_2 sorption isotherms of **Co-MOF-β** at 273, 283 and 298 K.

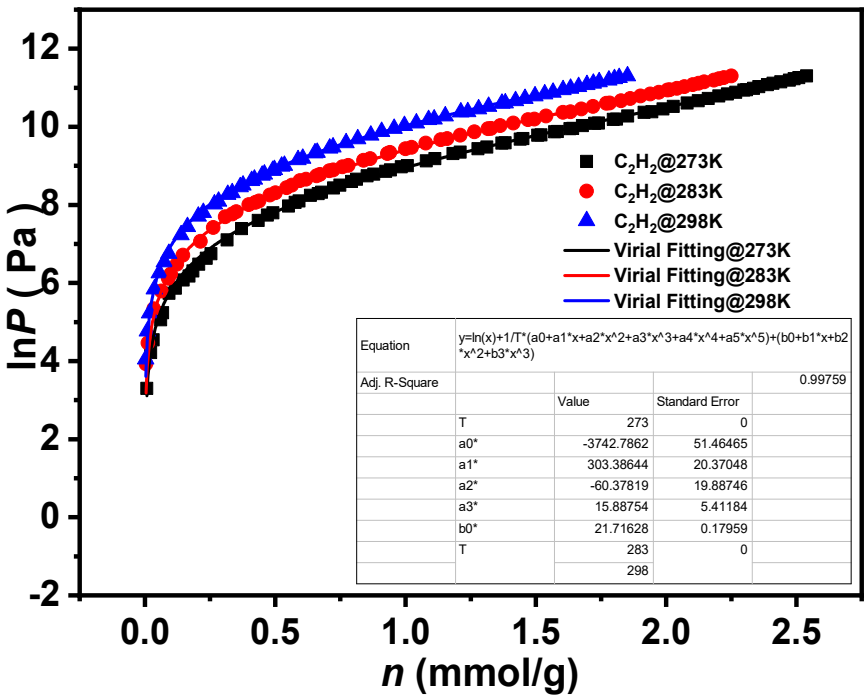

Equation	y=ln(x)+1/T*(a0+a1*x+a2*x^2+a3*x^3+a4*x^4+a5*x^5)+(b0+b1*x+b2*x^2+b3*x^3)			
Adj. R-Square				0.99759
		Value	Standard Error	
	T	273	0	
	a0*	-3742.7862	51.46465	
	a1*	303.38644	20.37048	
	a2*	-60.37819	19.88746	
	a3*	15.88754	5.41184	
	b0*	21.71628	0.17959	
	T	283	0	
		298		

Figure S30. The virial fitting of C_2H_2 sorption data for **Co-MOF-*β*** at 273, 283 and 298 K.

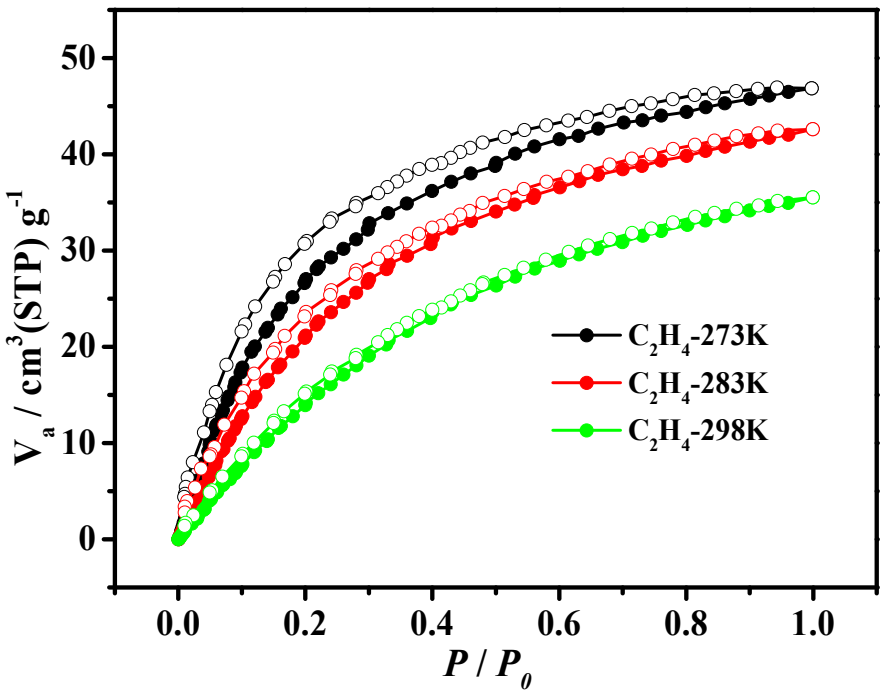

Figure S31. C_2H_4 sorption isotherms of **Co-MOF-*β*** at 273, 283 and 298 K.

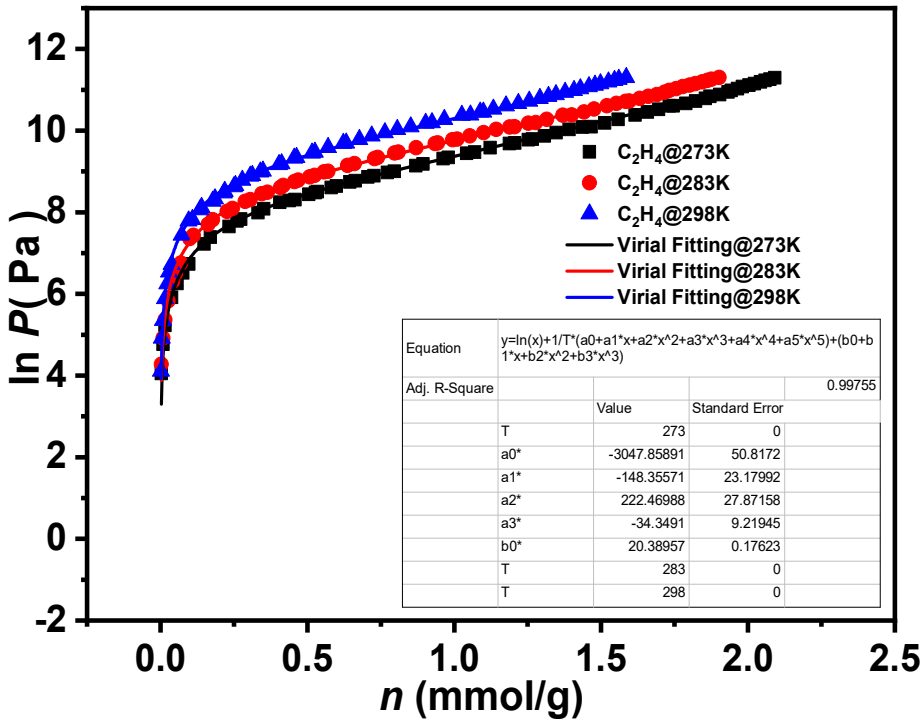

Figure S32. The virial fitting of C_2H_4 sorption data for **Co-MOF-*β*** at 273, 283 and 298 K.

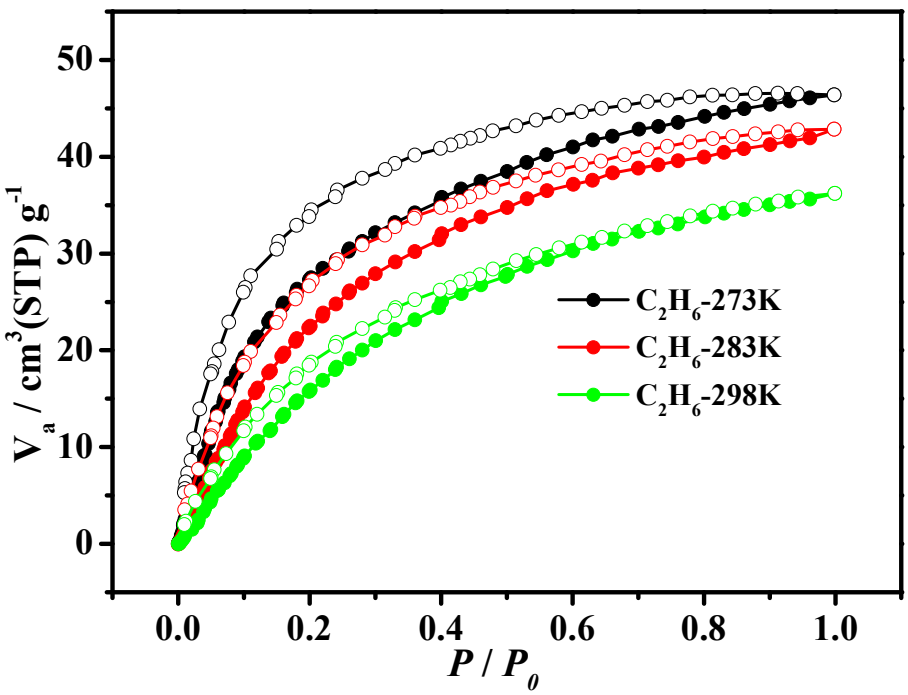

Figure S33. C_2H_6 sorption isotherms of **Co-MOF-*β*** at 273, 283 and 298 K.

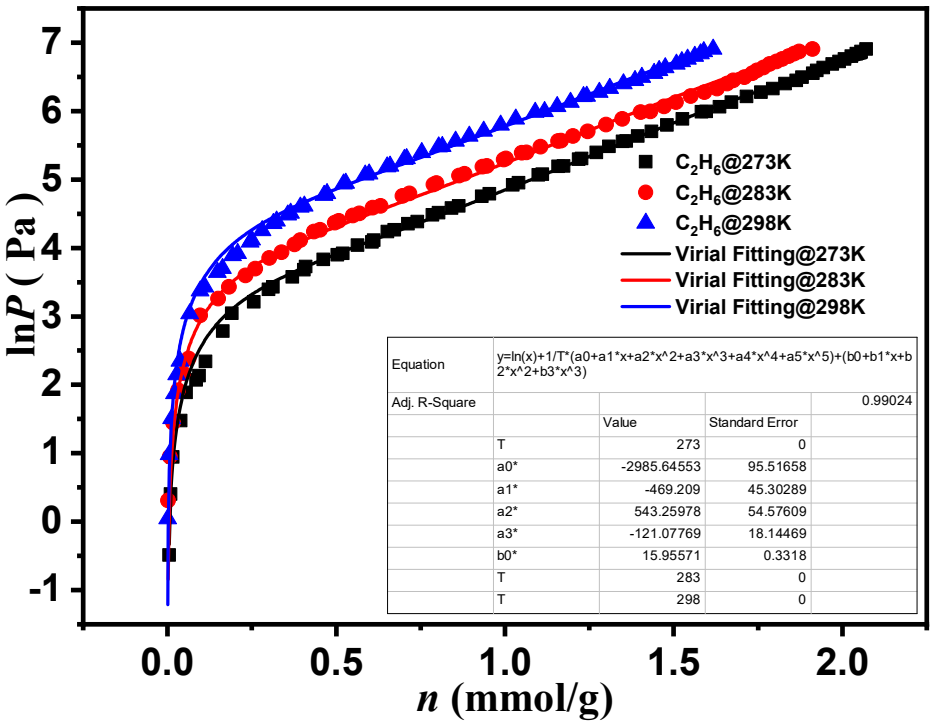

Equation	y=ln(x)+1/T*(a0+a1*x+a2*x^2+a3*x^3+a4*x^4+a5*x^5)+(b0+b1*x+b2*x^2+b3*x^3)			
Adj. R-Square				0.99024
		Value	Standard Error	
	T	273	0	
	a0*	-2985.64553	95.51658	
	a1*	-469.209	45.30289	
	a2*	543.25978	54.57609	
	a3*	-121.07769	18.14469	
	b0*	15.95571	0.3318	
	T	283	0	
	T	298	0	

Figure S34. The virial fitting of C_2H_6 sorption data for **Co-MOF-*β*** at 273, 283 and 298 K.

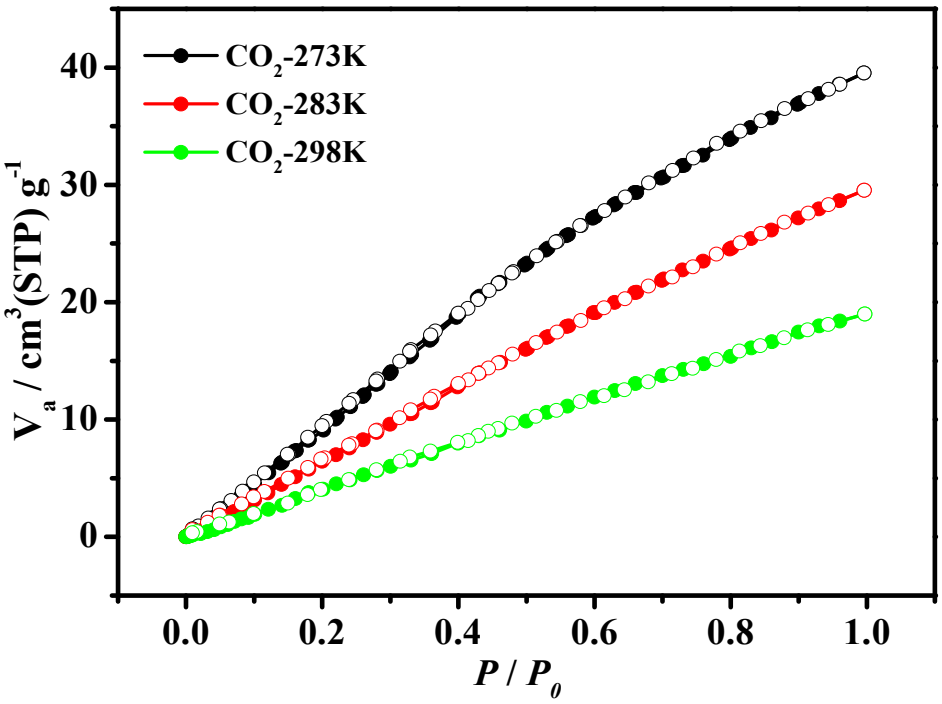

Figure S35. CO_2 sorption isotherms of **Co-MOF-*β*** at 273, 283 and 298 K.

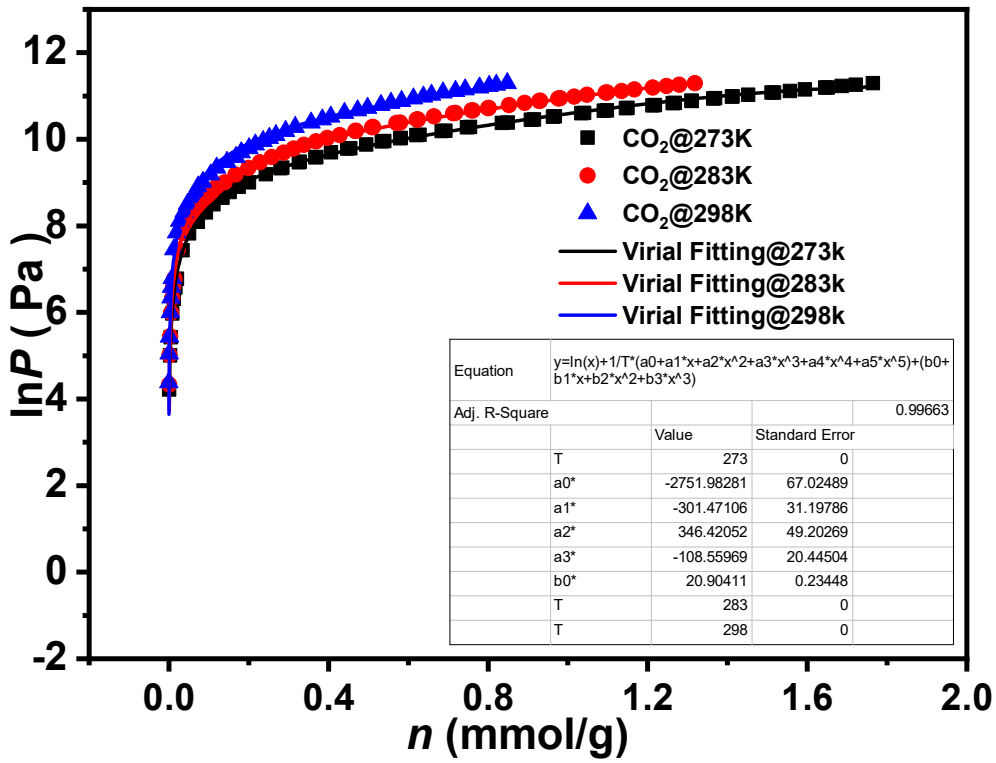

Equation	y=ln(x)+1/T*(a0+a1*x+a2*x^2+a3*x^3+a4*x^4+a5*x^5)+(b0+b1*x+b2*x^2+b3*x^3)			
Adj. R-Square				0.99663
		Value	Standard Error	
	T	273	0	
	a0*	-2751.98281	67.02489	
	a1*	-301.47106	31.19786	
	a2*	346.42052	49.20269	
	a3*	-108.55969	20.44504	
	b0*	20.90411	0.23448	
	T	283	0	
	T	298	0	

Figure S36. The virial fitting of CO_2 sorption data for **Co-MOF-*β*** at 273, 283 and 298 K.

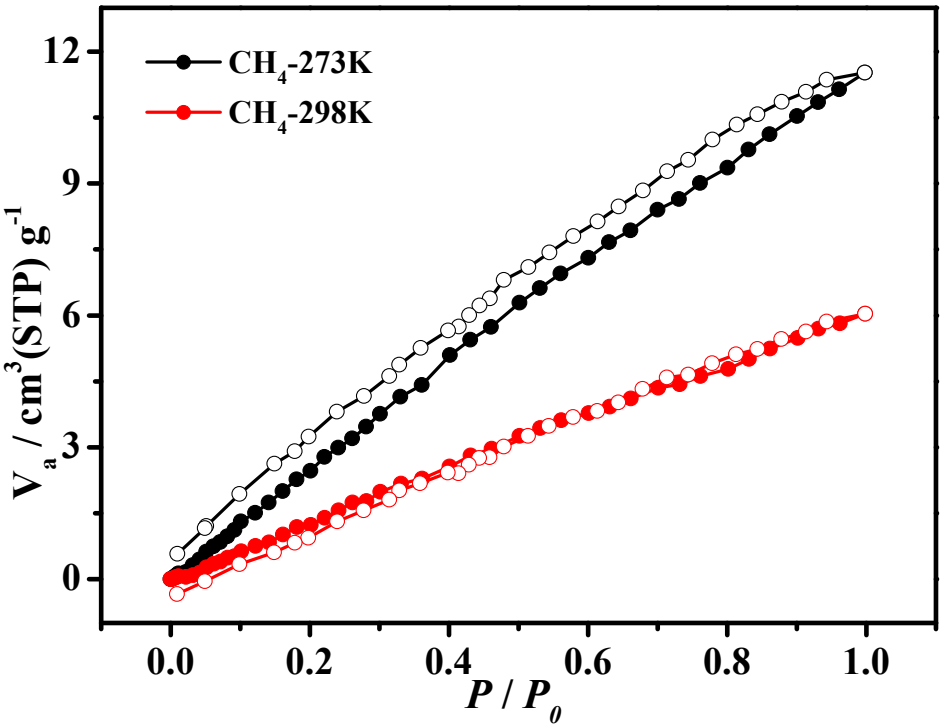

Figure S37. CH_4 sorption isotherms of **Co-MOF-*β*** at 273 and 298 K.

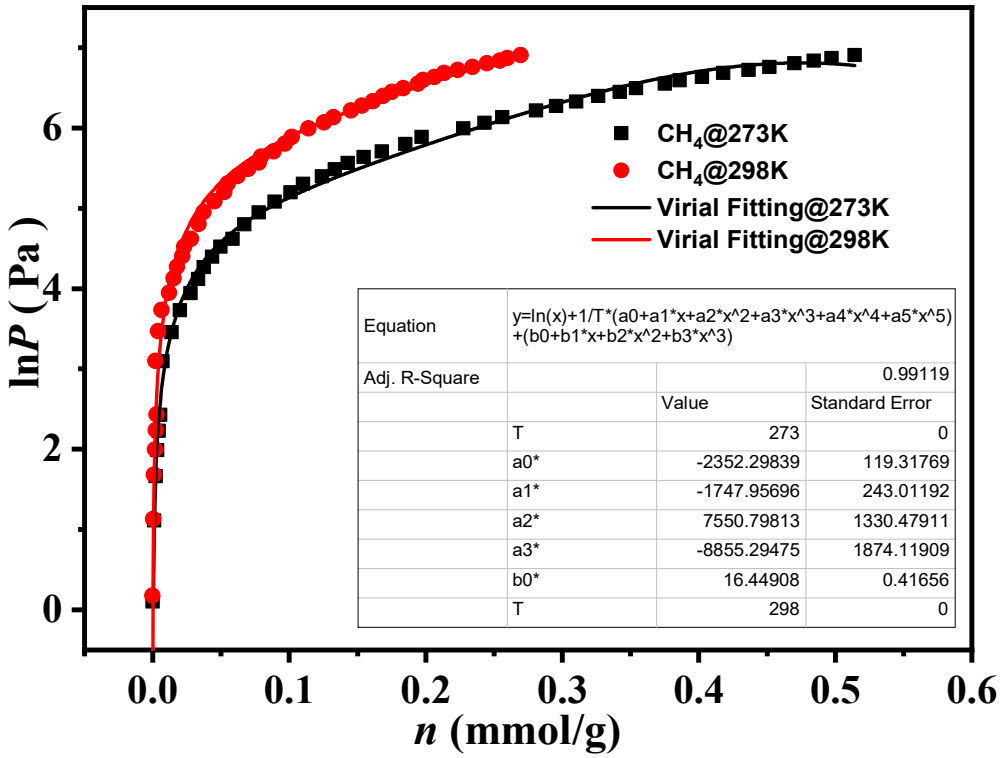

Equation	y=ln(x)+1/T*(a0+a1*x+a2*x^2+a3*x^3+a4*x^4+a5*x^5)+(b0+b1*x+b2*x^2+b3*x^3)		
Adj. R-Square			0.99119
		Value	Standard Error
	T	273	0
	a0*	-2352.29839	119.31769
	a1*	-1747.95696	243.01192
	a2*	7550.79813	1330.47911
	a3*	-8855.29475	1874.11909
	b0*	16.44908	0.41656
	T	298	0

Figure S38. The virial fitting of CH_4 sorption data for **Co-MOF-*β*** at 273 and 298 K.

15. Prediction of the gas adsorption selectivity by IAST

The ideal adsorption solution theory (IAST) was used to predict the binary mixture adsorption from the experimental pure gas isotherms. Single-component gas equilibrium adsorption isotherms were fitted with dual-site Langmuir–Freundlich (DSLF) model, given by the following equation:

$$N = A_1 \frac{b_1 p^{c_1}}{1 + b_1 p^{c_1}} + A_2 \frac{b_2 p^{c_2}}{1 + b_2 p^{c_2}}$$

where N is the amount of adsorbed gas (mmol g^{-1}), p is the bulk gas phase pressure (atm), A_1 and A_2 are the adsorption saturation capacity for site 1 and site 2 (mmol/g), b_1 and b_2 is the affinity coefficients of site (1/kPa), c_1 and c_2 is the Langmuir–Freundlich exponent (dimensionless) for two adsorption sites A and B indicating the presence of weak and strong adsorption sites.

The parameters of A_1, A_2, b_1, b_2 and c_1, c_2 were then used to predict the adsorption selectivity based on IAST, which is finally defined as:

$$S_{1/2} = (\frac{x_1}{x_2})(\frac{y_2}{y_1})$$

In equation, S is the ideal selectivity of component 1 over component 2, where x_i and y_i are the mole fractions of component i (i = 1 and 2) in the adsorbed and bulk phases, respectively.

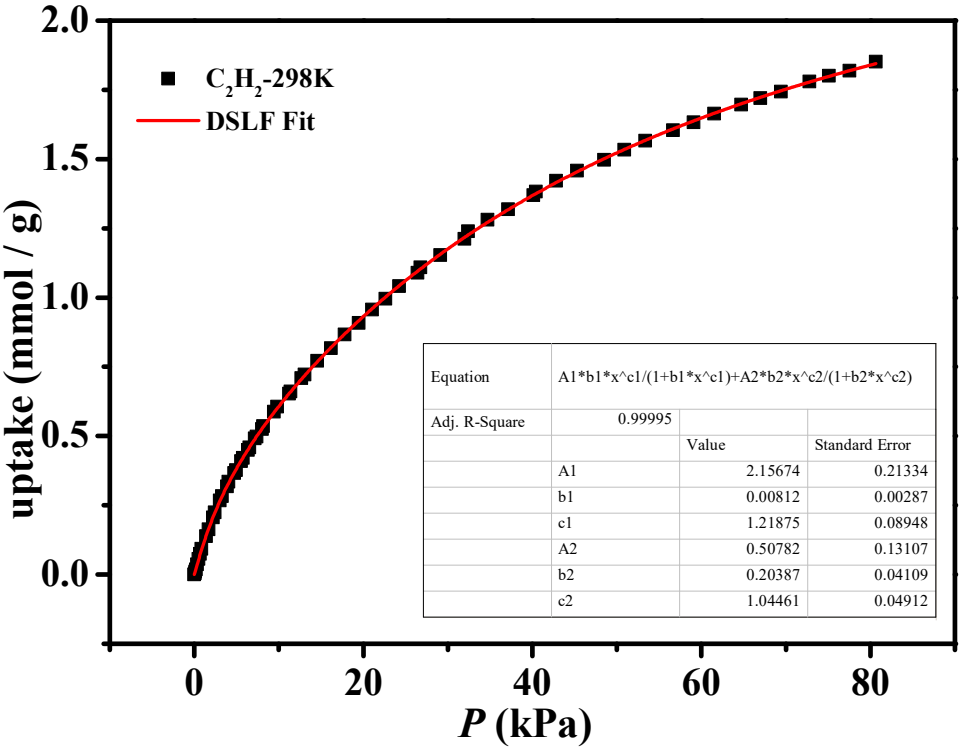

Figure S39. The dual-site Langmuir-Freundlich fitting of C_2H_2 sorption data for **Co-MOF-*β***.

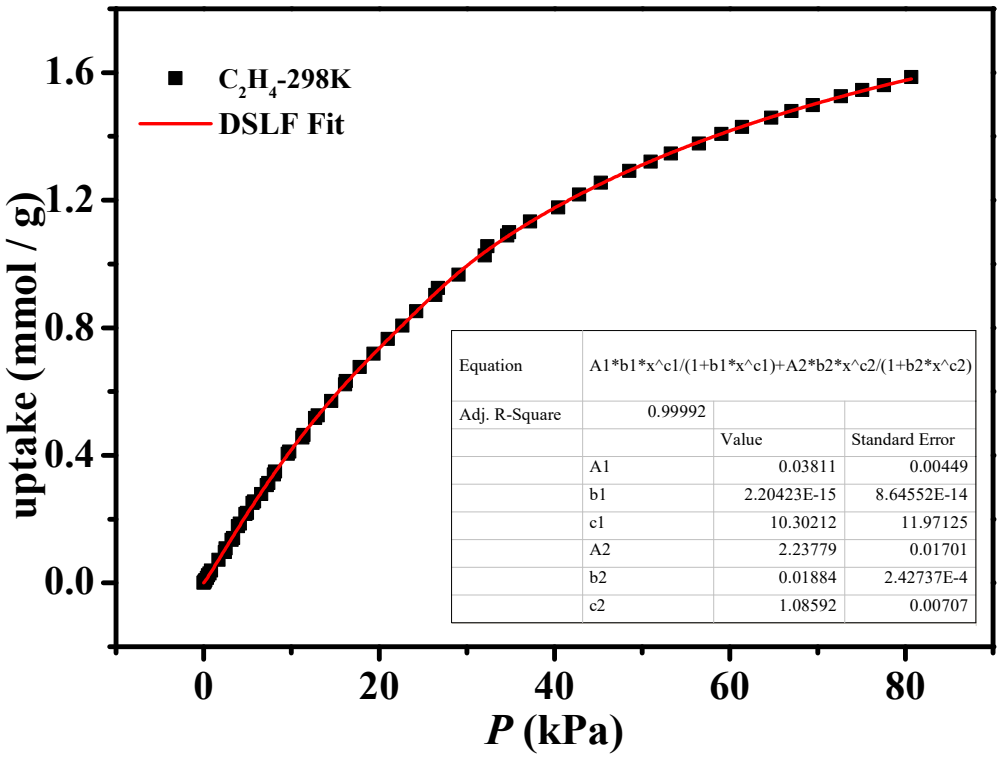

Figure S40. The dual-site Langmuir-Freundlich fitting of C_2H_4 sorption data for **Co-MOF-*β***.

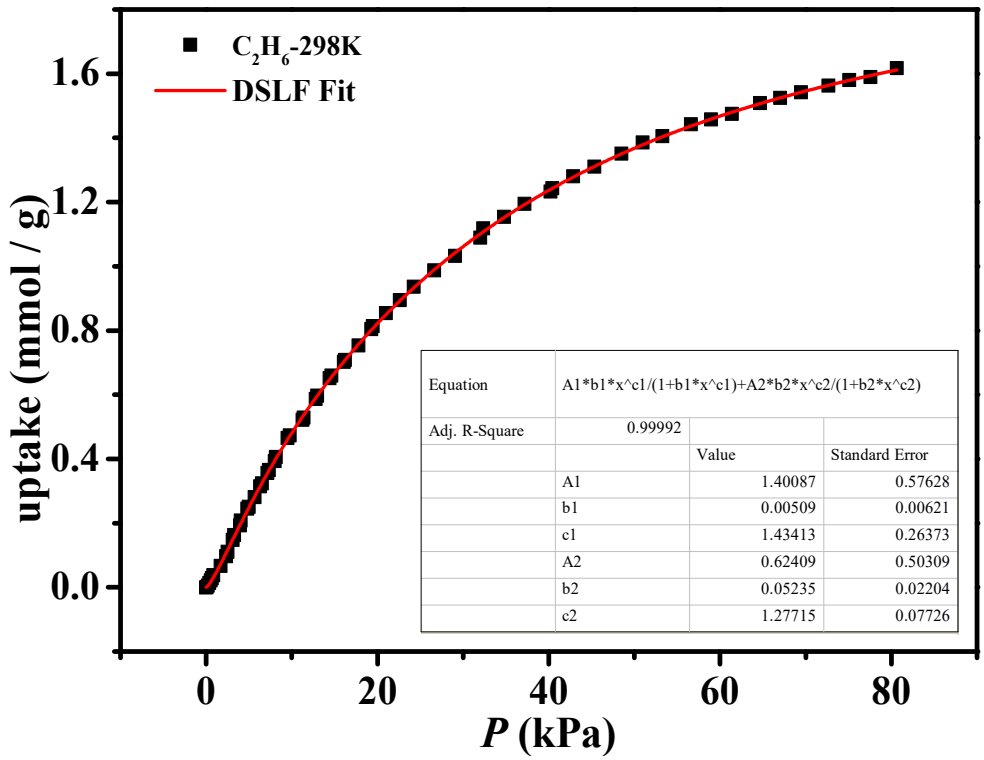

Figure S41. The dual-site Langmuir-Freundlich fitting of C_2H_6 sorption data for **Co-MOF-*β***.

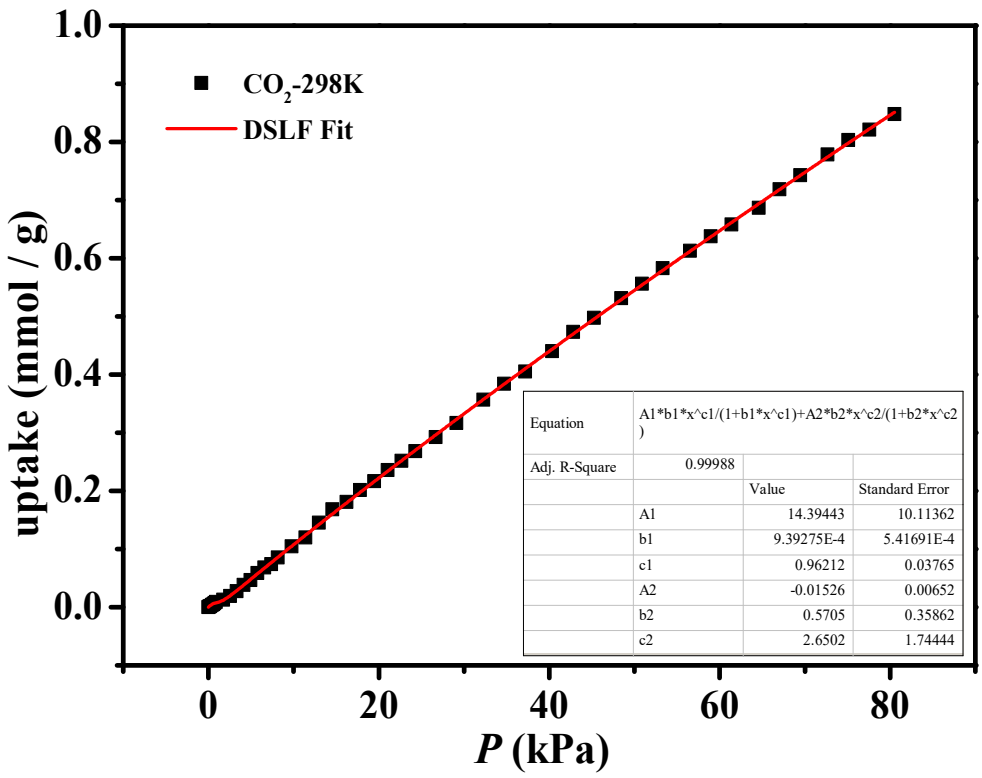

Figure S42. The dual-site Langmuir-Freundlich fitting of CO_2 sorption data for **Co-MOF-*β***.

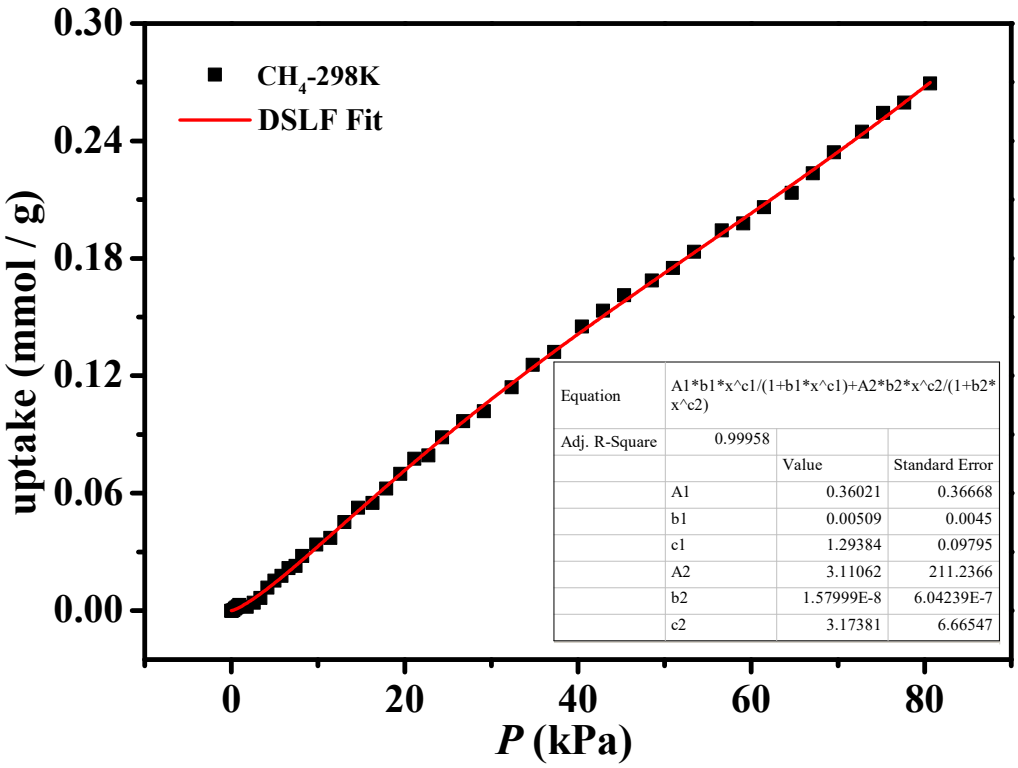

Figure S43. The dual-site Langmuir-Freundlich fitting of CH_4 sorption data for **Co-MOF-*β***.

16. Summary of gas adsorption and separation properties for metal-organic frameworks

Table S8. Summary of switching adsorbent materials with single-step type F-IV adsorption isotherms for C2 hydrocarbons.

Materials	Dimension	Triggered gas	Saturated Uptake (cm^3/g)	Pressure of gate opening	Ref.
Co-MOF-β	2D	C_2H_2	149 (195 K)[a]	$P/P_0 = 0.03$	This work
	2D	C_2H_4	130 (195 K)[a]	$P/P_0 = 0.10$	
	2D	C_2H_6	119 (195 K)[a]	$P/P_0 = 0.19$	
diarylethene MOF	3D	C_2H_2	120 (195 K)[a]	$P/P_0 = 0.02$	5
[Mn(bdc)(dpe)]	0D	C_2H_2	86 (195 K)[a]	$P/P_0 = 0.02$	6
Co(VTTF)	3D	C_2H_4	110 (170K)[a]	$P/P_0 = 0.09$	7
			31 (273K)[a]	$P/P_0 = 0.57$	
X-pcu-5-Zn-β	3D	C_2H_2	174 (195 K)[a]	$P/P_0 = 0.10$	8
	3D	C_2H_4	148 (195 K)[a]	$P/P_0 = 0.45$	
X-pcu-6-Zn-β	3D	C_2H_2	176 (195 K)[a]	$P/P_0 = 0.06$	
	3D	C_2H_4	147 (195 K)[a]	$P/P_0 = 0.30$	
X-pcu-7-Zn-β	3D	C_2H_2	180 (195 K)[a]	$P/P_0 = 0.12$	
	3D	C_2H_4	150 (195 K)[a]	$P/P_0 = 0.49$	
X-pcu-8-Zn-β	3D	C_2H_2	173 (195 K)[a]	$P/P_0 = 0.28$	
	3D	C_2H_4	72 (195 K)[a]	$P/P_0 = 0.82$	
$[Zn_2(sdb)_2(bpy)$	2D	C_2H_4	13 (195 K)[a]	$P/P_0 = 0.01$	9
	2D	C_2H_6	7 (195 K)[a]	$P/P_0 = 0.10$	
$Cu(BF_4)_2(bpp)_2$	1D	C_2H_6	72 (298 K)[b]	$P \approx 105$ kPa	10
$Zn(5NO_2\text{-ip})(dpe)$	3D	C_2H_4	48 (273 K)[b]	$P = 400$ kPa	11
	3D	C_2H_4	32 (298 K)[b]	$P = 720$ kPa	
NTU-65	3D	C_2H_2	110 (195 K)[a]	$P/P_0 \approx 0.001$	12
			86 (263 K)[a]	$P/P_0 = 0.012$	
			75 (298 K)[a]	$P/P_0 = 0.10$	
			68 (313 K)[a]	$P/P_0 = 0.20$	
			50 (333 K)[a]	$P/P_0 = 0.42$	
			95 (195 K)[a]	$P/P_0 \approx 0.10$	
DUT-8(Ni)	3D	C_2H_4	360 (169 K)[a]	$P/P_0 \approx 0.20$	13
		C_2H_6	350 (185 K)[a]	$P/P_0 \approx 0.20$	
$Zn_2(bpdc)_2(bpee)$	3D	C_2H_6	18 (298 K)[a]	$P/P_0 \approx 0.40$	14
$Mn(ina)_2$	3D	C_2H_6	28 (278 K)[a]	$P/P_0 \approx 0.20$	15
MOF-508	3D	C_2H_2	90 (290 K)[a]	$P/P_0 \approx 0.67$	16

[a] low pressure; [b] high pressure

Table S9. Summary of isosteric heat of adsorption (Q_{st}) of C_2H_2 for a series of metal-organic frameworks.

Materials	Dimension	Using methods	Q_{st} / KJ·mol^{-1}	Ref.
Co-MOF-β	2D	virial methods	31.1	This work
UPC-200(Al)-F-BIM	3D	virial methods	20.5	17
FJU-36a	3D	virial methods	32.9	18
Cu-CPAH	3D	virial methods	35.4	19
SNNU-37(Fe)	3D	virial methods	34.4	20
SNNU-37(Sc)	3D	virial methods	26.5	
UTSA-74a	3D	Clausius–Clapeyron equation	31.0	21
SNNU-45	3D	virial methods	38.4	22
UTSA-222a	3D	virial methods	26.0	23
ZJNU-100	3D	Clausius–Clapeyron equation	35.0	24
UTSA-38	3D	virial methods	24.7	25
ZnSDB	3D	Clausius–Clapeyron equation	23.1	26
UTSA-36a	2D	virial methods	29.0	27
Cu(BDC-OH)	2D	virial methods	25.7	28
MOF1a	3D	virial methods	28.2	29
$Zn_5(BTA)_6(TDA)_2$	3D	virial methods	37.3	30
Fe-MOF	3D	virial methods	38.4	31
Cr-MOF	3D	virial methods	36.8	
ZJU-30	3D	virial methods	31.3	32
UTSA-100a	3D	Clausius–Clapeyron equation	22.0	33
HKUST-1	3D	virial methods	30.4	34
ZJU-8	3D	virial methods	29.6	35
JMOF-2	2D	virial methods	68.5	36
IITKGP-20	2D	Clausius–Clapeyron equation	27.2	37

Table S10. A comparison of various MOFs materials used for selective adsorption for C_2H_2 over CO_2 and CH_4 at 1 atm.

Materials	Dimension	temperature	*v*/*v*	Adsorption selectivity		Ref.
				C_2H_2/CO_2	C_2H_2/CH_4	
Co-MOF-*β*	2D	298 K	50:50	4.5 [a]	8.8 [a]	This work
UPC-200(Fe)-F-BIM	3D	298 K	50:50	2.94 [a]	/	17
UPC-200(Fe)-F-H_2O	3D	298 K	50:50	2.25 [a]	/	
UPC-200(Fe)-F-IM	3D	298 K	50:50	2.71 [a]	/	
UPC-200(Fe)-F-MIM	3D	298 K	50:50	2.61 [a]	/	
UPC-200(Fe)-F-PY	3D	298 K	50:50	2.44 [a]	/	
UPC-200(Al)-F-H_2O	3D	298 K	50:50	2.53 [a]	/	
UPC-200(Cr)-F-H_2O	3D	298 K	50:50	2.31 [a]	/	
UPC-200(Ga)-F-H_2O	3D	298 K	50:50	2.39 [a]	/	
UPC-200(In)-F-H_2O	3D	298 K	50:50	2.35 [a]	/	
FJU-36a	3D	296 K	50:50	2.8 [a]	17.7 [a]	18
Cu-CPAH	3D	298 K	50:50	3.6 [a]	20.3 [a]	19
SNNU-37(Fe)	3D	298 K	50:50	9.9 [a]	/	20
SNNU-37(Sc)	3D	298 K	50:50	2.7 [a]	/	
UTSA-74a	3D	298 K	50:50	9.0 [a]	/	21
SNNU-45	3D	298 K	50:50	4.5 [a]	/	22
UTSA-222a	3D	296 K	50:50	4.0 [a]	16 [a]	23
ZJNU-100	3D	298 K	50:50	3.81 [a]	22.2 [a]	24
UTSA-38	3D	295K	50:50	/	5.6 [b]	25
ZnSDB	3D	298 K	50:50	/	16.9 [a]	26
UTSA-36a	2D	296K	50:50	/	13.8 [b]	27
Cu(BDC-OH)	2D	296K	50:50	/	9.26 [b]	28
MOF1a	3D	295K	50:50	/	14.7 [b]	29
$Zn_5(BTA)_6(TDA)_2$	3D	295 K	50:50	/	15.5 [a]	30
Fe-MOF	3D	298 K	50:50	5.7 [a]	2.9 [a]	31
Cr-MOF	3D	298K	50:50	3.5 [a]	3.1 [a]	
JMOF-2	2D	298K	50:50	12 [a]	/	36
IITKGP-20	2D	295K	50:50	/	53.1 [a]	37
FJU-90a	3D	298 K	50:50	4.3 [a]	/	38
UTSA-30a	3D	296 K	50:50	3.4 [a]	/	39
QMOF-1a	3D	298 K	50:50	/	13.5 [a]	40
$Cu(SiF_6)(sdi)_2$	3D	298 K	50:50	/	11.2 [a]	41
UTSA-10	3D	296 K	50:50	/	6.2 [b]	42
[$Zn_2(NH_2$-BTB)(2-nim)]	3D	273K	50:50	/	5 [a]	43
ZJU-16a	3D	298K	50:50	/	13 [a]	44
UPC-33	3D	298K	50:50	/	7.78 [a]	45
QMOF-2	3D	298K	50:50	/	5.3 [a]	46
JUN-4a	3D	298 K	50:50	8.2 [a]	/	47

FJI-H8-^{i}Pr	3D	298 K	50:50	5.35 [a]		48
SNNU-23	3D	298 K	50:50	/	17.4 [a]	49
Ca-MOF	3D	298 K	50:50	/	8.1 [a]	50
$(NH_2Me_2)_2Co_4(L)_2(\mu_2\text{-}OH)_2$	3D	298 K	50:50	/	14.5 [a]	51
$Cu(SiF_6)(sdi)_2$	3D	298 K	50:50	/	11.2 [a]	52
CPOC-101α	3D	298 K	50:50	11.9 [a]	/	53
sql-SIFSIX-bpe-Zn-β	3D	298 K	50:50	8.4 [a]	/	54
SIFSIX-22-Zn	3D	298 K	50:50	6.49 [a]	/	55
DZU-1	3D	298 K	50:50	6.1 [a]	/	56

[a] IAST selectivity; [b] selectivity from Henry's Law

References:

1. T. Higashi, *ABSCOR, Program for bruker area detector absorption correction*, Rigaku Corporation, Tokyo, Japan, 1995.
2. G. M. Sheldrick, *SADABS, A program for area detector absorption corrections*, University of Göttingen, Germany, 1994.
3. G. M. Sheldrick, *SHELXS-97, Program for the Solution of Crystal Structure*, University of Göttingen, Germany, 1997.
4. A. L. Spek, *PLATON, Molecular Geometry Program*, University of Utrecht, The Netherlands, 1999.
5. C. B. Fan, L. Le Gong, L. Huang, F. Luo, R. Krishna, X. F. Yi, A. M. Zheng, L. Zhang, S. Z. Pu, X. F. Feng, M. B. Luo and G. C. Guo, *Angew. Chem., Int. Ed*., 2017, **56**, 7900-7906.
6. M. L. Foo, R. Matsuda, Y. Hijikata, R. Krishna, H. Sato, S. Horike, A. Hori, J. Duan, Y. Sato, Y. Kubota, M. Takata, and S. Kitagawa, *J. Am. Chem. Soc*., 2016, **138**, 3022-3030.
7. S. Sen, N. Hosono, J. J. Zheng, S. Kusaka, R. Matsuda, S. Sakaki and S. Kitagawa, *J. Am. Chem. Soc*., 2017, **139**, 18313-18321.
8. A. X. Zhu, Q. Y. Yang, S. Mukherjee, A. Kumar, C. H. Deng, A. A. Bezrukov, M. Shivanna and M. J. Zaworotko, *Angew. Chem., Int. Ed*., 2019, **58**, 18212-18217.
9. Y. Hijikata, S. Horike, M. Sugimoto, M. Inukai, T. Fukushima and S. Kitagawa, *Inorg. Chem*., 2013, **52**, 3634-3642.
10. S.-i. Noro, R. Ochi, Y. Inubushi, K. Kubo and T. Nakamura, *Micropor. Mesopor. Mater.*, 2015, **216**, 92-96.
11. S. Horike, K. Kishida, Y. Watanabe, Y. Inubushi, D. Umeyama, M. Sugimoto, T. Fukushima, M. Inukai and S. Kitagawa, *J. Am. Chem. Soc*., 2012, **134**, 9852-9855.
12. Q. Dong, X. Zhang, S. Liu, R. B. Lin, Y. Guo, Y. Ma, A. Yonezu, R. Krishna, G. Liu, J. Duan, R. Matsuda, W. Jin and B. Chen, *Angew. Chem., Int. Ed.,* 2020, **59**, 22756-22762.
13. V. Bon, N. Klein, I. Senkovska, A. Heerwig, J. Getzschmann, D. Wallacher, I. Zizak, M. Brzhezinskaya, U. Mueller and S. Kaskel, *Phys. Chem. Chem. Phys*., 2015, **17**, 17471-17479.
14. N. Nijem, H. Wu, P. Canepa, A. Marti, K. J. Balkus, Jr., T. Thonhauser, J. Li and Y. J. Chabal, *J. Am. Chem. Soc*., 2012, **134**, 15201-15204.
15. D. Banerjee, H. Wang, A. M. Plonka, T. J. Emge, J. B. Parise, and J. Li, *Chem.-Eur. J*., 2016, **22**, 11816-11825.
16. S. C. Xiang, W. Zhou, J. M. Gallegos, Y. Liu, and B.l. Chen, *J. Am. Chem. Soc*., 2009, **131**, 12415-12419.
17. W. D. Fan, S. Yuan, W. J. Wang, L. Feng, X. P. Liu, X. R. Zhang, X. Wang, Z. X. Kang, F. N. Dai, D. Q. Yuan, D. F. Sun, and H. C. Zhou, *J. Am. Chem. Soc*., 2020, **142**, 8728-8737.
18. L. Liu, Z. Yao, Y. Ye, L. Chen, Q. Lin, Y. Yang, Z. Zhang and S. Xiang, *Inorg. Chem*., 2018, **57**, 12961-12968.
19. L. Meng, L. Yang, C. Chen, X. Dong, S. Ren, G. Li, Y. Li, Y. Han, Z. Shi and S. Feng, *ACS. Appl. Mater. Inter*., 2020, **12**, 5999-6006.

20. S. C. Fan, Y. T. Li, Y. Wang, J. W. Wang, Y. Y. Xue, H. P. Li, S. N. Li and Q. G. Zhai, *Inorg. Chem*., 2021, **60**, 18473-18482.
21. F. Luo, C. Yan, L. Dang, R. Krishna, W. Zhou, H. Wu, X. Dong, Y. Han, T. L. Hu, M. O'Keeffe, L. Wang, M. Luo, R. B. Lin and B. Chen, *J. Am. Chem. Soc*., 2016, **138**, 5678-5684.
22. Y. P. Li, Y. Wang, Y. Y. Xue, H. P. Li, Q. G. Zhai, S. N. Li, Y. C. Jiang, M. C. Hu and X. Bu, *Angew. Chem., Int. Ed*., 2019, **131**, 13724-13729.
23. J. X. Ma, J. Guo, H. Wang, B. Li, T. Yang and B. Chen, *Inorg. Chem*., 2017, **56**, 7145-7150.
24. Y. Wang, M. He, X. Gao, X. Wang, G. Xu, Z. Zhang and Y. He, *Inorg. Chem.*, 2019, **6**, 263-270.
25. M. C. Das, H. Xu, Z. Wang, G. Srinivas, W. Zhou, Y. F. Yue, V. N. Nesterov, G. Qian and B. Chen, *Chem. Commun.,* 2011, **47**, 11715-11717.
26. F. S. Tang, R.-B. Lin, R.-G. Lin, J. C.-G. Zhao and B. Chen, *J. Solid State Chem*., 2018, **258**, 346-350.
27. M. C. Das, H. Xu, S. Xiang, Z. Zhang, H. D. Arman, G. Qian and B. Chen, *Chem.-Eur. J.*, 2011, **17**, 7817-7822.
28. Z. Chen, S. Xiang, H. D. Arman, P. Li, S. Tidrow, D. Zhao and B. Chen, *Eur. J. Inorg. Chem*., 2010, 3745-3749.
29. Z. Zhang, S. Xiang, X. Rao, Q. Zheng, F. R. Fronczek, G. Qian and B. Chen, *Chem. Commun*., 2010, **46**, 7205-7207.
30. Z. Zhang, S. Xiang, Y. S. Chen, S. Ma, Y. Lee, T. Phely-Bobin and B. Chen, *Inorg. Chem*., 2010, **49**, 8444-8448.
31. T. T. Lu, Y. Y. Fan, X. N. Wang, Q. Wang and B. Li, *Dalton Trans*., 2022, **51**, 11658-11664.
32. J. Cai, J. Yu, H. Xu, Y. He, X. Duan, Y. Cui, C. Wu, B. Chen and G. Qian, *Cryst. Growth Des*., 2013, **13**, 2094-2097.
33. T. L. Hu, H. Wang, B. Li, R. Krishna, H. Wu, W. Zhou, Y. Zhao, Y. Han, X. Wang, W. Zhu, Z. Yao, S. Xiang and B. Chen, *Nat. Commun*., 2015, **6**, 7328.
34. S. C. Xiang, W. Zhou, J. M. Gallegos, Y. Liu and B. Chen, *J. Am. Chem. Soc*., 2009, **131**, 12415-12419.
35. J. Cai, H. Wang, H. Wang, X. Duan, Z. Wang, Y. Cui, Y. Yang, B. Chen and G. Qian, *RSC Adv*. 2015, **5**, 77417-77422.
36. W. Gong, H. Arman, Z. Chen, Y. Xie, F. A. Son, H. Cui, X. Chen, Y. Shi, Y. Liu, B. Chen, O. K. Farha and Y. Cui, *J. Am. Chem. Soc*., 2021, **143**, 657-663.
37. R. Sahoo, S. Chand, M. Mondal, A. Pal, S. C. Pal, M. K. Rana and M. C. Das, *Chem.-Eur. J.*, 2020, **26**, 12624-12631.
38. Y. Ye, Z. Ma, R. B. Lin, R. Krishna, W. Zhou, Q. Lin, Z. Zhang, S. Xiang and B. Chen, *J. Am. Chem. Soc*., 2019, **141**, 4130-4136.
39. Y. He, S. Xiang, Z. Zhang, S. Xiong, F. R. Fronczek, R. Krishna, M. O'Keeffe and B. Chen, *Chem. Commun.,* 2012, **48**, 10856-10858.
40. R. G. Lin, R. B. Lin and B. Chen, *J. Solid State Chem*., 2017, **252**, 138-141.
41. Y. P. Xia, C. X. Wang, M. H. Yu and X. H. Bu, *Chinese Chem. Lett*., 2021, **32**, 1153-1156.
42. Y. He, C. Song, Y. Ling, C. Wu, R. Krishna and B. Chen, *APL Mater*., 2014, **2**, 124102.
43. Q. R. Ding and F. Wang, *Dalton Trans*., 2016, **45**, 7004-7007.
44. X. Duan, R. Lv, Z. Ji, B. Li, Y. Cui, Y. Yang and G. Qian, *Inorg. Chem*., 2018, **5**, 1193-1198.
45. W. Fan, Y. Wang, Q. Zhang, A. Kirchon, Z. Xiao, L. Zhang, F. Dai, R. Wang and D. Sun, *Chem.-Eur. J.*, 2018, **24**, 2137-2143.
46. Y. Guo, C. Liang, C. C. Zhang, J. Ferrando-Soria, Y. Gao, J. H.Yang, X. Y. Liu and E Pardo, *Chem.-Asian J*., 2022, **17**, e202101220.
47. H. Zeng, X. J. Xie, Y. Wang, D. Luo, R. J. Wei, W. Lu and D. Li, *Chem. Sci*., 2022, **13**, 12876-12882.
48. Z. Di, C. Liu, J. Pang, C. Chen, F. Hu, D. Yuan, M. Wu and M. Hong, *Angew. Chem., Int. Ed.,* 2021, **60**, 10828-10832.
49. J. W. Zhang, M. C. Hu, S. N. Li, Y. C. Jiang and Q. G. Zhai, *Dalton Trans*., 2017, **46**, 836-844.
50. M. Chen and Z.-W. Wang, *Polyhedron*., 2021, **208**,115438
51. T. Ding, J.-R. Chen, J.-J. Chen, Z.-Y. Li, D. Gao, L.-N. Zheng and Z.-W. Gao, *J. Solid State Chem*., 2022, **305**,122629.
52. Y.-P. Xia, C.-X. Wang, M.-H. Yu and X.-H. Bu, *Chin. Chem. Lett*., 2021, **32**, 1153-1156.
53. W. Wang, K. Su, E.-S. M. El-Sayed, M. Yang and D. Yuan, *ACS Appl. Mater. Interfaces*, 2021, **13**, 24042-24050.

54. M. Shivanna, K. I. Otake, B. Q. Song, L. M. van Wyk, Q. Y. Yang, N. Kumar, W. K. Feldmann, T. Pham, S. Suepaul, B. Space, L. J. Barbour, S. Kitagawa and M. J. Zaworotko, *Angew. Chem., Int. Ed.,* 2021, **60**, 20383-20390.
55. D. Sensharma, D. J. O'Hearn, A. Koochaki, A. A. Bezrukov, N. Kumar, B. H. Wilson, M. Vandichel and M. J. Zaworotko, *Angew. Chem., Int. Ed.,* 2022, **61**, e202116145.
56. B. Y. Zhu, T. Zhang, C. H. Li, J. W. Cao, Z. Q. Zhang, W. Qi, G. Y. Wang, Z. H. Rong, Y. Wang and K. J. Chen, *Inorg. Chem*., 2022, **61**, 4555-4560.